

Sulfur Vacancy Related Optical Transitions in Graded Alloys of $\text{Mo}_x\text{W}_{1-x}\text{S}_2$ Monolayers

Mahdi Ghafariasl¹, Tianyi Zhang², Zachary D. Ward³, Da Zhou⁴, David Sanchez²,
Venkataraman Swaminathan⁵, Humberto Terrones³, Mauricio Terrones^{2,4,6}, Yohannes Abate^{1*}

¹ Department of Physics and Astronomy, University of Georgia, Athens, Georgia 30602, USA

² Department of Materials Science and Engineering, The Pennsylvania State University,
University Park, PA 16802, USA

³ Department of Physics and Astronomy, Rensselaer Polytechnic Institute, Rensselaer, New York
12180, USA

⁴ Department of Physics, The Pennsylvania State University, University Park, PA 16802, USA

⁵ Department of Materials Science and Nanoengineering, Rice University, Houston, TX 77005,
USA

⁶ Department of Chemistry, The Pennsylvania State University, University Park, PA 16802, USA

*Corresponding author E-mail: yohannes.abate@uga.edu

ABSTRACT

Engineering the electronic bandgap is of utmost importance in diverse domains ranging from information processing and communication technology to sensing and renewable energy applications. Transition metal dichalcogenides (TMDCs) provide an ideal platform for achieving this goal through techniques including alloying, doping, and creating in-plane or out-of-plane heterostructures. Here, we report on the synthesis and characterization of atomically controlled

two-dimensional graded alloy of $\text{Mo}_x\text{W}_{1-x}\text{S}_2$, wherein the center region is Mo rich and gradually transitions towards a higher concentration of W atoms at the edges. This unique alloy structure leads to a continuously tunable bandgap, ranging from 1.85 eV in the center to 1.95 eV at the edges consistent with the larger band gap of WS_2 relative to MoS_2 . Aberration-corrected high-angle annular dark-field scanning transmission electron microscopy showed the presence of sulfur monovacancy, V_S , whose concentration varied across the graded $\text{Mo}_x\text{W}_{1-x}\text{S}_2$ layer as a function of Mo content with the highest value in the Mo rich center region. Optical spectroscopy measurements supported by *ab initio* calculations reveal a doublet electronic state of V_S , which was split due to the spin-orbit interaction, with energy levels close to the conduction band or deep in the band gap depending on whether the vacancy is surrounded by W atoms or Mo atoms. This unique electronic configuration of V_S in the alloy gave rise to four spin-allowed optical transitions between the V_S levels and the valence bands. Our work highlights the potential of simultaneous defect and optical engineering of novel devices based on these 2D monolayers.

KEYWORDS

Two-dimensional materials, Transition Metal Dichalcogenides, Alloying, Doping, Heterostructures, Photoluminescence, Excitons, Defects, Sulfur Vacancy

INTRODUCTION

Bandgap engineering is of great importance in modern semiconductor technology because of its capability for tuning the materials' optical and electrical properties that are key to their applications. In the past decade, the emergence of atomically-thin two-dimensional (2D) layered materials have provided an open canvas to engineer their bandgaps for device applications such as

tunable lasers, light-emitting diodes (LEDs), and nanoelectronics^{1,2}. Among the family of 2D materials³⁻⁵, monolayers of semiconducting transition metal dichalcogenides (TMDCs), such as MoS₂ and WSe₂⁶, possess direct bandgaps at optical frequencies, making them excellent candidates for bandgap engineering via diverse approaches such as alloying, hetero-stacking, strain engineering, intercalation, temperature control, and applying external electric fields⁷⁻¹⁵. Compared to bandgap tuning approaches that rely on external applied factors (e.g., temperature, strain, and electric field), alloying provides an effective and stable control because the bandgap is controlled by the intrinsic chemical composition, and a continuous bandgap engineering can be achieved by precisely modulating the alloy composition^{16,17}. To date, ternary alloys of monolayer TMDCs (e.g., Mo_xW_{1-x}S₂, MoS_{2x}Se_{2(1-x)}) have been achieved by means of chemical vapor deposition (CVD)^{18,19}, physical vapor deposition (PVD)^{20,21}, exfoliation of bulk crystals synthesized by chemical vapor transport (CVT)²², and other methods, allowing for the access of tunable optical properties as a function of compositions.

We employed an alkali metal halide-assisted CVD method to synthesize alloyed Mo_xW_{1-x}S₂ monolayers that showcase intriguing compositional gradients within individual crystals, and we thoroughly examined their optical properties. The alloys exhibit distinct compositional gradient transitioning from a Mo-rich center to a W-rich periphery. This strategically controlled alloying within a single crystal enabled the spatial tuning of the bandgap in a wide range (by over 0.1 eV), characterized by a uniform radial emission profile spanning across the entire flake, and facilitated the investigation of continuously composition-dependent intralayer optical transitions. Examining the defect structure in the alloy using aberration-corrected high-angle annular dark-field scanning transmission electron microscopy (AC-HAADF-STEM) showed the presence of sulfur

monovacancy, V_S , whose concentration varied across the graded $\text{Mo}_x\text{W}_{1-x}\text{S}_2$ layer as a function of Mo content with the highest value in the Mo rich center region and the lowest value in the W rich edges. Detailed spectral analysis of the photoluminescence from the alloy as a function of temperature (4K-300K) and laser excitation intensity suggested several intralayer optical transitions besides the intrinsic band edge excitons. To investigate the origin of these transitions, detailed *ab initio* calculations were performed of the band structure of the alloy considering spin-orbit interactions. A doublet electronic state of V_S , which was split due to the spin-orbit interaction, was identified for the first time with energy levels close to the conduction band or deep in the band gap depending on whether the vacancy in the alloy is surrounded by W atoms or Mo atoms. This unique electronic configuration of V_S in the alloy gave rise to four spin-allowed optical transitions between the V_S levels and the valance bands. Matching the calculated transition energies with the peak positions of the deconvoluted peaks, enabled the identification of free-to-bound transitions involving a photoexcited electron captured at the doublet V_S level and a hole in the top of the valence band at $k=0$. In addition, bound exciton transitions associated with the V_S doublet were also identified. Thus, a multitude of V_S related intralayer optical transitions reported for the first time in the alloy $\text{Mo}_x\text{W}_{1-x}\text{S}_2$, reveals the complex interplay between composition and defect structure thereby providing the exciting opportunity of combined defect and optical engineering to realize novel devices in alloyed TMDCs.

RESULTS AND DISCUSSION

Sample Synthesis and characterization

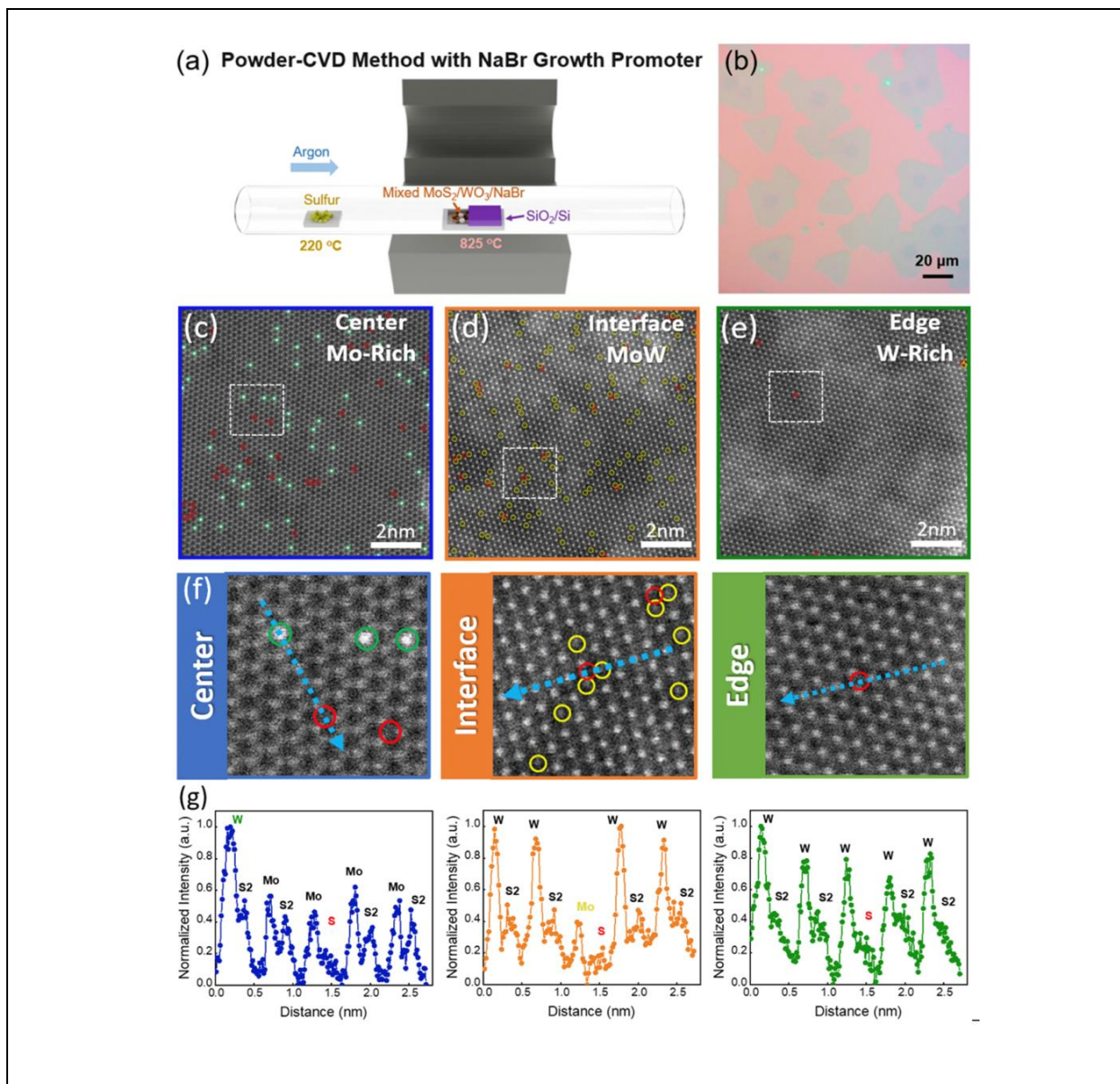


Figure 1. The synthesis of Alloyed $\text{Mo}_x\text{W}_{1-x}\text{S}_2$ and AC-HRSTEM Structural Characterization (a) A schematic of the synthesis of alloyed $\text{Mo}_x\text{W}_{1-x}\text{S}_2$ monolayers with center-to-edge composition gradient. (b) Optical image of as-grown $\text{Mo}_x\text{W}_{1-x}\text{S}_2$ monolayer on SiO_2/Si substrate. (c–e) Typical AC-HAADF-STEM images acquired from the center, interface, and edge areas of the $\text{Mo}_x\text{W}_{1-x}\text{S}_2$ monolayer. The red, green and yellow circles denote the sulfur monovacancy (V_S), W atoms, and Mo atoms, respectively. (f) magnified images of the white dash boxes at the center, interface, and edge areas of the $\text{Mo}_x\text{W}_{1-x}\text{S}_2$ monolayer. (g) The corresponding intensity line profiles of areas marked by the blue arrows in (f) for three different regions of the alloyed $\text{Mo}_x\text{W}_{1-x}\text{S}_2$ monolayer.

Additive-assisted CVD has recently emerged as a powerful method for the preparation of 2D TMDCs and their heterostructures²³. The use of growth additives, such as alkali metal halides (e.g., NaCl, NaBr) and organic compounds with aromatic structures (e.g., reduced graphene oxide (rGO), perylene-3,4,9,10-tetracarboxylic acid tetra potassium salt (PTAS)), can effectively promote the growth of TMDCs with enhanced yield, increased grain sizes, and improved uniformity of layer numbers and morphology²⁴⁻²⁶. In our work, we employed an additive-assisted synthesis technique to prepare single-crystalline monolayers of alloyed $\text{Mo}_x\text{W}_{1-x}\text{S}_2$. An alkali metal halide-assisted CVD method was applied, with mixed MoS_2 and WO_3 powders as transition metal precursors and NaBr as a growth promoter (Figure 1(a)). An optical image of typical as-grown $\text{Mo}_x\text{W}_{1-x}\text{S}_2$ alloys is displayed in Fig. 1(b), showing truncated-triangular morphologies with noticeable optical contrast differences from center to edge regions. Unlike the in-plane heterostructures synthesized by liquid-phase precursor-assisted approach, which we previously reported^{27,28}, this method produced alloyed $\text{Mo}_x\text{W}_{1-x}\text{S}_2$ monolayers with center-to-edge composition gradient (a schematic is shown in Fig. 2(a)), similar to graded TMDC alloys synthesized previously²⁹⁻³¹. Z-contrast aberration-corrected high angle annular dark field scanning transmission electron microscopy (AC-HAADF-STEM) imaging of the $\text{Mo}_x\text{W}_{1-x}\text{S}_2$ monolayer revealed that the Mo and W concentrations varied continuously from the center to the edge of the flake. The center regions contain a higher Mo concentration compared to the edge regions which are dominated by W with a compositional gradient interface between the two regions. This observation was further confirmed using far-field Raman and photoluminescence (PL) studies as discussed below. AC-HAADF-STEM imaging further identified that V_S is the prevalent point defect in alloyed $\text{Mo}_x\text{W}_{1-x}\text{S}_2$ monolayers, which is labeled by the red-colored circles in Figs. 1(c)-(e). The center, interface, and edge regions contain estimated V_S defect densities of 0.185 nm^{-2} ,

0.091 nm⁻², 0.023 nm⁻², respectively. We note that there is a relationship between the prevalent transition metal (Mo or W) and the density of V_S. The center, which has the highest Mo concentration, also has the highest density of V_S. In contrast, the edge, which has the highest W concentration, has the lowest density of V_S. In the interface region, between the center and edge regions, we observed a V_S density bounded by the two regions. The V_S densities for the Mo-rich center and W-rich edge regions are in accordance with defect densities previously measured in CVD-grown MoS₂ and WS₂ monolayers^{32,33}.

Optical Characterization of alloyed Mo_xW_{1-x}S₂ at room temperature

To characterize the structural and optical properties of as-synthesized TMDC alloys, we performed far-field Raman and PL measurements. Figures 2(b) and 2(e) illustrate the Raman spectra acquired from different regions of Mo_xW_{1-x}S₂ alloys. The material exhibits Raman signatures that are consistent with the previous results, with MoS₂-like vibrational modes dominating in center regions and WS₂-like vibrational modes in edge regions, while the interface/middle regions exhibit a combination of both sets of modes^{30,27}. The PL emissions from the center (~1.85 eV) and edge regions (~1.95 eV) of the alloyed structure are close to the optical band gap of pristine MoS₂ and WS₂, respectively (Fig. 2(c)).

To further elucidate the structural and optical property differences of the sample as a function of position within the flake, Raman and PL line scans were performed on a representative alloyed monolayer Mo_xW_{1-x}S₂ flake along the scan direction marked in Fig. 2(d) and plotted in Figs. 2(e) and (f). The intensities of both the convoluted WS₂ E' and 2LA(M) modes (black line) and the MoS₂ E' mode (red line) display a gradual change along the scan direction (Fig. 2(e)), which unambiguously indicates a composition gradient from center to edge of the flake. Consequently,

the optical band gap of the alloyed $\text{Mo}_x\text{W}_{1-x}\text{S}_2$ was continuously modulated due to the lateral variation of the degree of alloying, indicated by the gradual change in PL peak positions (Fig. 2(f)) that is consistent with previous results on graded TMDC alloys^{29,34}. We also map the band edge emission spatial profile of the $\text{Mo}_x\text{W}_{1-x}\text{S}_2$ alloy by taking hyperspectral PL imaging²⁸. Figure 2(g) shows 3D hyperspectral data cube taken by measuring an array of 75 by 75 pixels PL normalized spectra of the alloyed monolayer. The x and y axes of the 3D data cube shown in Fig. 2(g) indicate the plane of the sample surface while the z-axis corresponds to the photon energy axis (1.85 to 2.0 eV). The acquisition time for each spectrum was 1 sec, and total acquisition time of 2 h per image (see Materials and Methods for details). The PL spatial map at a fixed energy is extracted by cross-section cut of the cube as shown in Fig. 2(h).

The energy dependent PL emission maps reveal 2D quasi-symmetric spatial variation of the degree of alloying from the center to the edge of the flake. In general, the energy gap of an alloy A_xB_{1-x} in terms of the pure compound energy gap E_A and E_B , follows an equation³⁵

$$E(x) = E_B + (E_A - E_B - b)x + bx^2 \quad (1)$$

Where b is the bowing parameter. For $\text{Mo}_x\text{W}_{1-x}\text{S}_2$ fitting PL peak positions to the above equation Chen et al.³⁰, obtained a b value of 0.25 eV for the A exciton peak and 0.19 eV for the B exciton peak. However, for the alloys $\text{AB}_{2(1-x)}\text{C}_{2x}$ where both B and C are chalcogen atoms, the bowing was found to be considerably smaller¹⁷. As the alloy composition is not directly determined in our samples, treating the scan position as a variable, and fitting the PL peaks in Fig. 2(f) to the above equation gives a value of $b \sim 0.054$ eV suggesting small bowing. From this we surmise that

the small bowing parameter indicates small lattice mismatch/strain and thermodynamic miscibility in our samples due to the unique CVD sample synthesis method employed in our study.

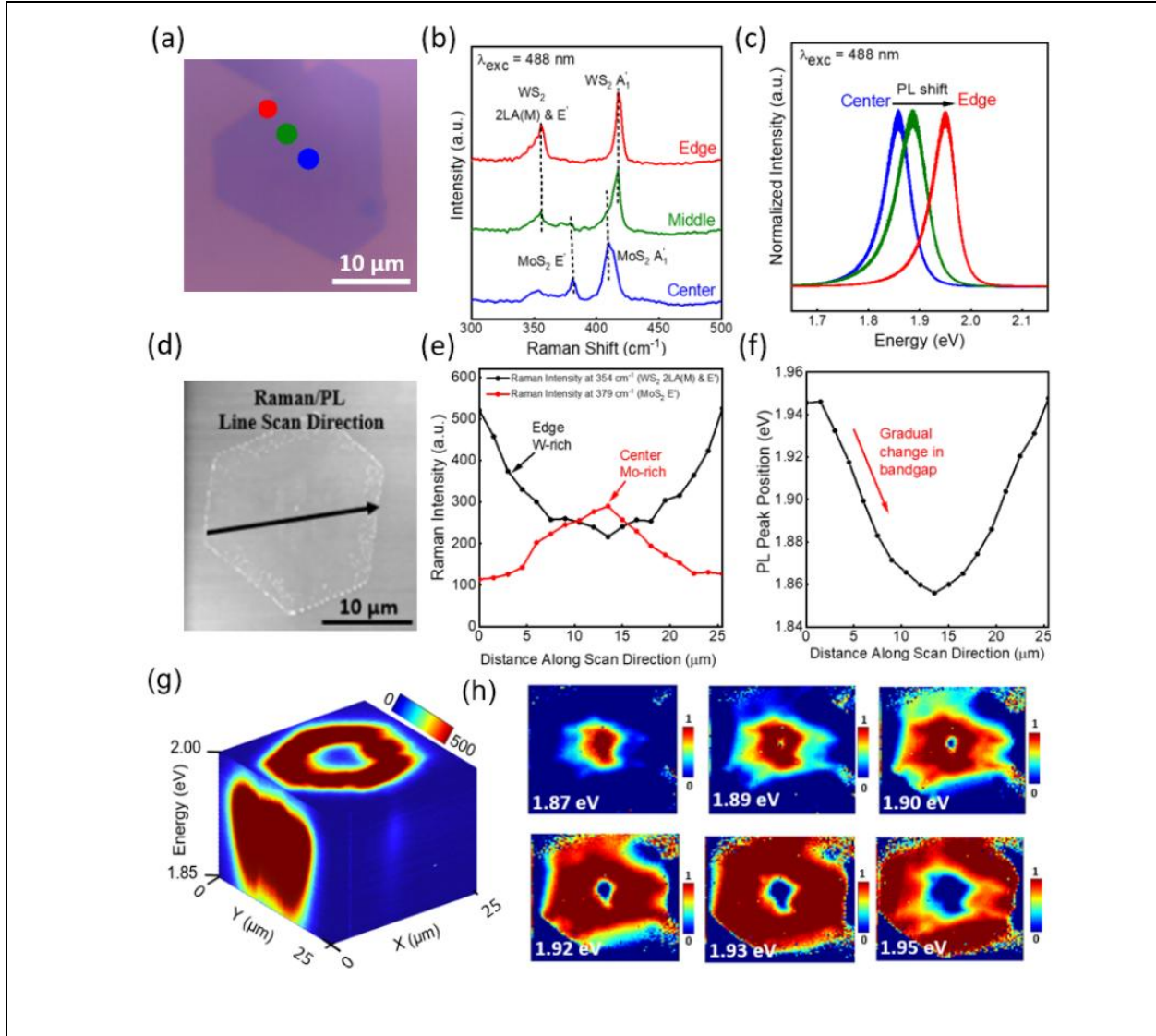


Figure 2. Optical Characterization of alloyed monolayer $\text{Mo}_x\text{W}_{1-x}\text{S}_2$. (a) Schematic of the structure of alloyed monolayer $\text{Mo}_x\text{W}_{1-x}\text{S}_2$. (b) Raman and (c) PL spectra of various regions in alloyed monolayer $\text{Mo}_x\text{W}_{1-x}\text{S}_2$. (d) Optical microscopy image of the $\text{Mo}_x\text{W}_{1-x}\text{S}_2$ flake used for Raman and PL line scans (the scan direction is marked by the black arrow). (e) Raman intensity profiles of WS_2 E' and 2LA(M) modes (black) and MoS_2 E' mode (red line) as a function of distance along the scan direction. Both Raman modes display gradual changes with scan

direction. (f) The evolution of PL peak positions of alloyed monolayer $\text{Mo}_x\text{W}_{1-x}\text{S}_2$ as a function of distance along the scan direction. The gradual shift in the peak position along the scan direction indicates spatially varying optical band gaps within the material. (g) 3D cube hyperspectral PL map. (h) Section cut images taken from the hyperspectral map at different energies.

Low-temperature photoluminescence of the alloyed monolayer $\text{Mo}_x\text{W}_{1-x}\text{S}_2$

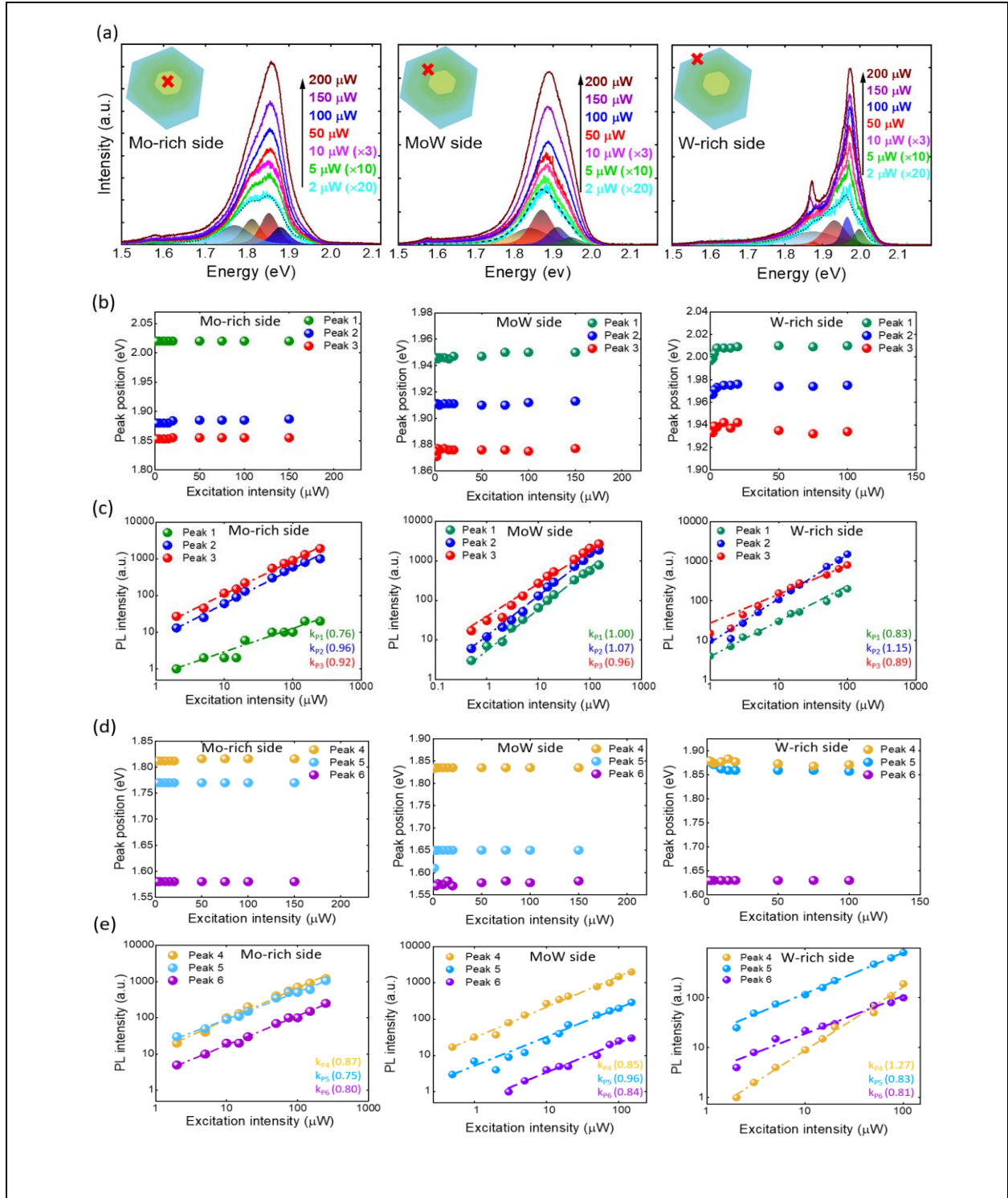


Figure 3. Laser excitation power dependence of the photoluminescence for the alloyed monolayer $\text{Mo}_x\text{W}_{1-x}\text{S}_2$ at $T=4\text{K}$. (a) shows the spectra from the center (Mo-rich side), intermediate region (MoW side), and edge (W-rich side). (b) Power dependence of the peak positions (peaks labeled 1-3) at the three regions. (c) PL intensity of peaks 1-3 at different

excitation powers at the three regions. (d) Power dependence of peak position for peaks 4-6 at the three regions. (e) PL intensity of peaks 4-6 at different excitation powers at the three regions.

The excitation power dependence of the PL intensities provide insight into the nature of the radiative recombination processes that give rise to the different spectral features near the band edge at different regions of the alloyed structure³⁶. To that end we performed laser excitation power-dependent PL spectroscopy at low temperature ($T=4$ K). Figure 3a shows the PL spectra of the $\text{Mo}_x\text{W}_{1-x}\text{S}_2$ alloy with data obtained at the W-rich edge region (region 3), Mo-rich center region (region 1), and the intermediate composition region (region 2) acquired using excitation laser power from in the range $2 \mu\text{W}$ to $200 \mu\text{W}$. Throughout the paper, the PL spectra for all powers and the three regions were deconvoluted using six pseudo-Voigt function peaks shown in the shaded colored representative spectra, which provide the best fit of the experimental data (Fig. 3a Peaks 2-5; peaks 1 & 6 are weaker compared to the other peaks and are not shown). Further representative spectra analysis is shown in Fig. S11 at the edge, center, and the intermediate composition regions using excitation laser power of $100 \mu\text{W}$ at 4K.

Near band edge peaks (1-3) in the three regions

In order to study the recombination mechanisms of different peaks in different regions of the alloyed $\text{Mo}_x\text{W}_{1-x}\text{S}_2$ monolayer, we have divided the fitted peaks into two main categories depending on their location relative to the band edges. Firstly, we selected peaks close to the band edges (peaks 1-3), then we chose peaks far away from those band edges (peaks 4-6). Figure 3b shows the peak positions for peaks 1-3 in three different regions of the alloyed monolayer as a function of excitation power to determine their origin. In the Mo-rich center region of the sample the highest energy peak (peak 1~ 2.02 eV) is weak for all the excitation powers. In this region, the

position of peaks 1-3 show negligible change with excitation power. For the intermediate MoW region, peaks 1-3 show a blue shift of ~ 2 meV with increasing excitation power. This shift can be considered negligible as it is within the uncertainties of the spectral fitting. In the W-rich side, the peak shifts are larger, ~ 4 meV for peak 1 and ~ 9 meV for peak 2. Peak 3 shows initially a blue shift (~ 9 meV) and then a red shift (~ 4 meV). As the density of the photoexcited carriers increases with increasing excitation power, the quasi-Fermi levels for electrons and holes shift respectively into the conduction and valence bands leading to a blue shift^{37,38}. However, other many-body interactions such as strain-induced band variation giving rise to reduced band gap and exciton binding energy would lead to a redshift of the excitonic peaks^{39,40}. For the low excitation powers used in our experiments presumably the carrier density is not high enough to give rise to the many-body interactions and the observed blue shifts are essentially caused by the shift of the quasi-Fermi levels.

To determine the physical origin of the different peaks in different regions of the alloyed semiconductor, power dependence of the integrated PL intensity of the various peaks are extracted. Figure 3c shows the PL intensity of peaks 1-3 as a function of excitation power using the power law $I=P^k$ fit where I , P , and k represent PL intensity, laser excitation intensity, and a numeric coefficient, respectively. Typically, free and bound excitons show a linear dependence of excitation power ($k=1$), biexcitons show a quadratic dependence ($k=2$), and sub-linear ($k<1$) dependence would indicate free-to-bound type of radiative transitions through impurities and defects⁴¹. The k values are indicated for the different peaks in Fig 3c. A three-particle center like a trion would be expected to show a superlinear dependence ($k=3/2$). However, if the trions dominate the radiative recombination process, which is likely at high excitation intensities, then a linear dependence ($k=1$) is expected⁴². As evidenced in Fig. 3c, peaks 1-3 show nearly a linear

dependence on excitation intensity in all the three regions. The low k value of 0.76 for peak 1 in Mo-rich side is attributed to the low PL intensity of the peak and the resultant uncertainties in the spectral fits. Based on the near linear dependence of the PL intensity on excitation intensity we surmise that the peaks 1-3 in all the regions are of excitonic origin.

By comparing the peak positions in Mo-rich side of the $\text{Mo}_x\text{W}_{1-x}\text{S}_2$ alloyed monolayer with the values reported for the A and B excitons in monolayer pristine MoS_2 (Table SI 2), we assign the peaks 1 (~ 2.01 eV) and 2 (~ 1.89 eV) in the Mo-rich side to the B and A excitons, respectively. Similarly, peak 1 in the W-rich side can be assigned to the A exciton. The B exciton in pristine WS_2 is generally much weaker than the A exciton and is rarely evidenced^{43,44} in PL measurements. Accordingly, by comparing peak 1 in W-rich region (~ 2.01 eV) with the values reported for the A exciton in monolayer WS_2 (Table SI 1), we assign it to the A excitonic transition in the W-rich side. Thus, the difference in the peak positions assigned to the A excitons in Mo-rich side and W-rich side is 120 meV which is comparable to the 100 meV PL shift observed at room temperature from center (Mo-rich side) to edge (W-rich side) (Fig. 2c) in the $\text{Mo}_x\text{W}_{1-x}\text{S}_2$. As the band gap increases from the Mo-rich side to the W-rich side, the A excitonic position will increase continuously from the center to the edge region, we can assign peak 1 in region 2 (intermediate MoW side) to the A exciton. Thus, the A exciton peaks vary from 1.89 eV (Mo-rich side) to 1.95 eV (intermediate MoW side) and to 2.01 eV (W-rich side). Assuming similar exciton binding energies, this is consistent with the increase of the band gap going from MoS_2 to WS_2 .

The near linear dependence of the PL intensities of the peak 3 (~ 1.86 eV, region 1), and peaks 2 (~ 1.91 eV, region 2) (~ 1.98 eV, region 3) as shown in Fig. 3c suggests they are of excitonic origin

as well. Peak 3 (region 1) and peak 2 (regions 2 & 3) are separated from the respective A exciton peaks by 29 ± 2 meV in region 1, and 36 ± 2 meV and 33 ± 2 meV in regions 2 and 3, respectively. Generally, the PL peak observed on the low energy side of the A exciton in TMDCs is attributed to radiative recombination involving a three-particle (an exciton with an electron or a hole) trion^{45,38}, with binding energies in the range 20-40 meV in pristine MoS₂ and 40-60 meV in pristine WS₂ (Tables SI 1 and SI 2). However, the expected $k \sim 3/2$ dependence on excitation intensity of the assigned trion peak has not been reported⁴². Further, the calculated trion binding energies for MoS₂ and WS₂ are roughly the same, of the order of 30 meV, and are also very sensitive to the dielectric environment⁴⁶. In an alloyed semiconductor such as Mo_xW_{1-x}S₂, the alloy disorder, if any, may also affect the trion binding energy. As shown in Fig. 3c, peak 3 (region 1) and peak 2 (regions 2 and 3) show $k \sim 1$ suggesting an excitonic recombination. A previous study in monolayer WS₂ assigned the peak on the low energy side, separated by ~ 29 -35 meV from the A exciton, to a bound excitonic transition³³. We conclude that peak 3 (region 1) and peak 2 (regions 2 & 3) are not trion-related transitions but are bound exciton transitions arising from the same impurity or defect in the alloyed Mo_xW_{1-x}S₂. Over the range of excitation powers used, peak 3 in region 2 (~ 1.88 eV) and region 3 (~ 1.93 eV) are separated by 71 ± 2 meV and 69 ± 5 meV, respectively, from the A exciton peak. This peak also shows linear dependence on excitation intensity implying a bound excitonic transition for its origin as well.

Peaks (4-6) far from the band edge in the three regions

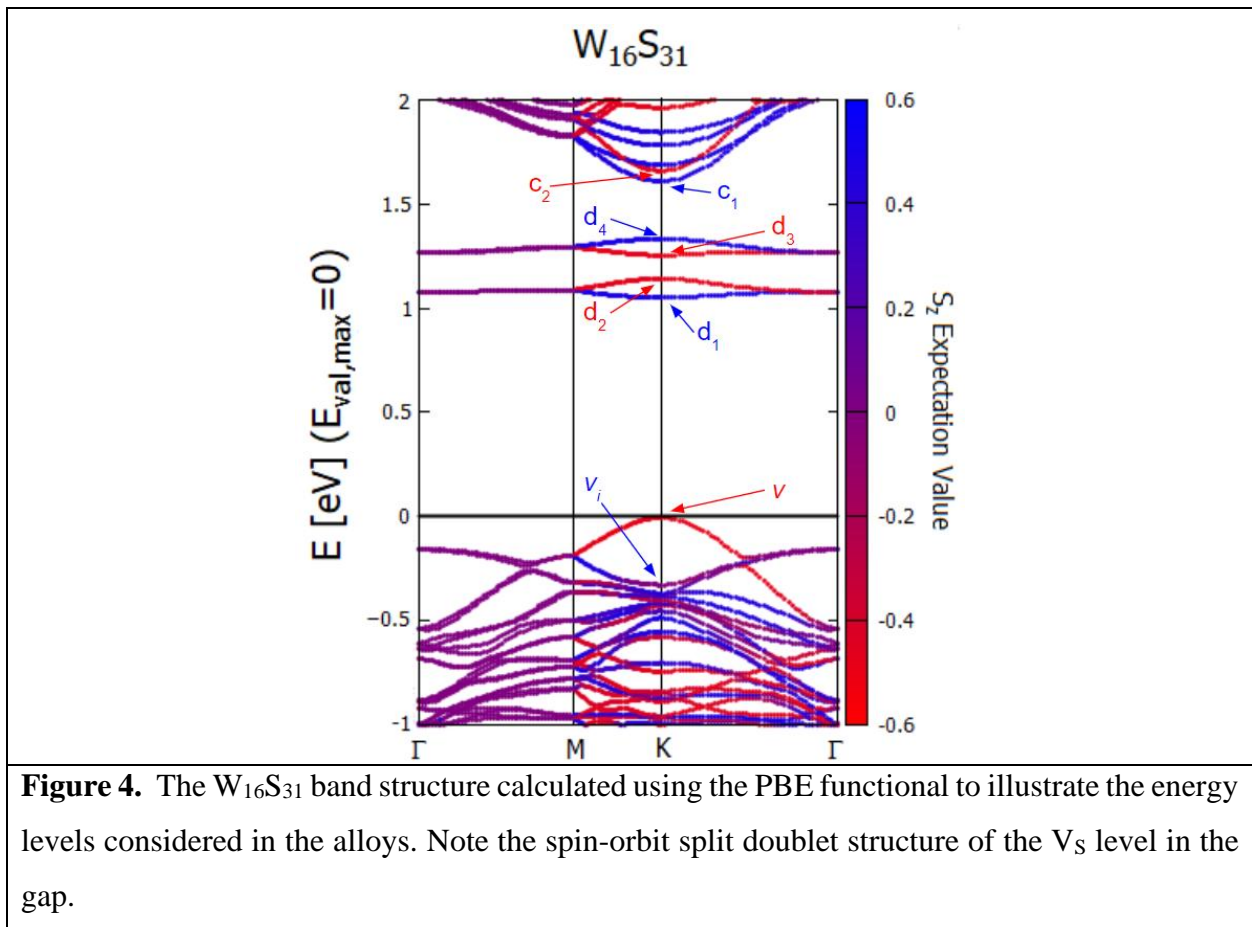
As shown in Fig. 3a, the PL spectra from Mo_xW_{1-x}S₂ show significant broadening on the low energy side in all the three regions. The spectral fitting of this region yields three additional peaks, labeled P4, P5 and P6. The dependence of these peaks, observed far from the band edge, on

excitation power is shown in Fig. 3d & 3e. The peaks generally show negligible shifts in their positions with increasing excitation power with the exception of peak 5 (~ 1.88 eV @ $1\mu\text{W}$; 1.857 eV @ $100\mu\text{W}$) in W-rich side which shows initially a red shift of ~ 20 meV and saturates above $20\mu\text{W}$. It is expected in an alloy semiconductor that upon increasing the excitation intensity the photoexcited carriers migrate to regions of lower bandgap due to compositional grading before recombination. However, since the other peaks do not show such a large red shift, it is likely that peak 5 arises from a localized region of compositional disorder in region 3.

DFT calculations

To assist in the analysis and assignment of the PL transitions observed at low temperature, we performed DFT calculations to identify the role of alloying on the electronic band structure and in particular, on the energy levels of the predominant defect center, namely sulfur vacancy, V_S . Most theoretical work regarding the spin-orbit coupling effect in TMDCs considered pristine MoS_2 and WS_2 , where the spin orbit splitting between the spin-up and spin-down states in WS_2 and MoS_2 monolayers are calculated to be 0.4 eV^{47,48} and 0.15 eV⁴⁹⁻⁵¹. This splitting effect is largely responsible for the production of the A and B excitons in these pristine samples^{52,53} (observed in PL spectra measurements due to spin-allowed bright excitonic transitions). While a few studies have used spin-orbit coupling for WS_2 and MoS_2 monolayers, there are not many studies involving the spin-orbit coupling effect with the V_S defect. When the V_S defect is considered, calculations reveal that the valence band splitting tends to decrease to 0.05 eV and 0.30 eV for both MoS_2 ^{54,55} and WS_2 ⁵⁶, respectively. STM imaging of the V_S defect has confirmed the valence band splitting for WS_2 to be 0.25 eV⁵⁶ while only theoretical calculations have been shown to yield a decrease in valence band splitting for MoS_2 with the V_S defect. The V_S defect introduces defect levels

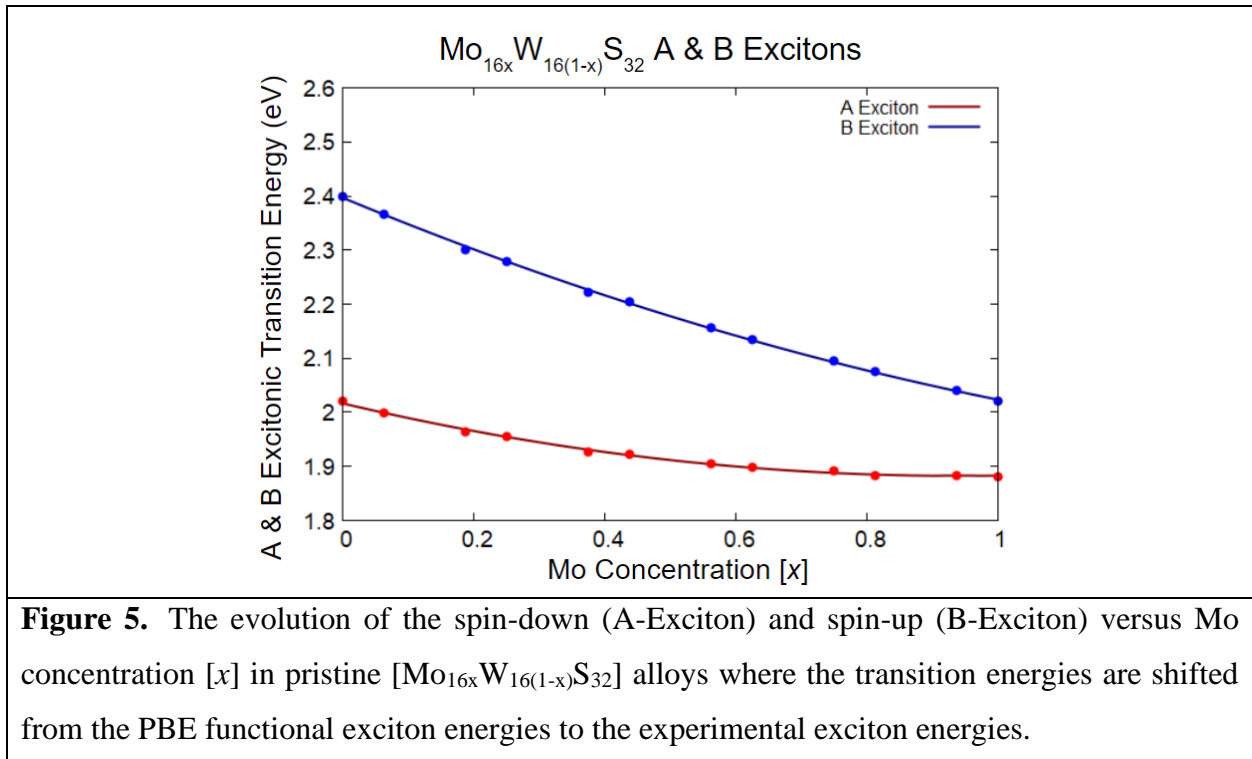
within the bandgap, which are radiative and can be attributed to the origin of PL peaks below the A exciton^{33,57}. Given that spin-orbit coupling has not been studied in $\text{Mo}_x\text{W}_{1-x}\text{S}_2$ alloys with varying Mo concentration, this study attempts to both understand the evolution of the A and B exciton and the V_S defect-mediated radiative transitions by investigating multiple possible configurations for the $\text{Mo}_x\text{W}_{1-x}\text{S}_2$ alloy and examine how by varying the positions and concentration of W and Mo atoms surrounding the V_S defect affects the optical transitions.



Sulfur vacancy, V_S levels (Computational Methods)

The energy levels are all considered at the K point with the distinct energy levels being denoted in the valence band, defect band, and conduction band (Fig. 4) with $\text{W}_{16}\text{S}_{31}$ as an example. In all

cases investigated, only the allowed transitions are considered. That is, the energy difference between bands of the same color (blue to blue and red to red) are allowed. The $v-c_2$ and v_i-c_1 transitions in the pristine alloys $[\text{Mo}_{16x}\text{W}_{16(1-x)}\text{S}_{32}]$ are attributed to the A and B excitons, respectively. The defect-mediated transitions ($v-d_2$, $v-d_3$, v_i-d_1 , and v_i-d_4) are obtained from the V_S hosting alloys $[\text{Mo}_{16x}\text{W}_{16(1-x)}\text{S}_{32}]$ and are studied to develop a model to predict the transition energies based on the geometry of the alloy. In addition, the valence (v_i-v) and conduction band splitting (c_1-c_2) are also studied. For pristine $\text{W}_{16}\text{S}_{32}$ and $\text{Mo}_{16}\text{S}_{32}$, the A (B) excitonic transition energies are underestimated and are measured to be 1.607 eV (2.001 eV) and 1.615 eV (1.759 eV), respectively, with conduction (valence) band splitting of 0.032 eV (0.426 eV) and 0.003 eV (0.147 eV), respectively. Given the transitions are underestimated, a scissor shift is performed to correct the A (B) exciton energies to the experimental energies of 1.88 eV (2.02 eV) and 2.02 (2.40 eV) for $\text{Mo}_{16}\text{S}_{32}$ and $\text{W}_{16}\text{S}_{32}$, respectively^{58,59}.



The evolution of the A exciton tends to decrease monotonically with the decrease in energy becoming less rapid as the Mo concentration $[x]$ increases (Fig. 5), which confirms with the observations seen in the experimental PL spectra measurements (Fig. 2, Tables SI 1-2). The 32 configurations investigated in this study are divided into three separate classes based on the Mo concentration $[x]$: Mo-rich ($x \geq 0.75$), MoW [intermediate region] ($0.25 < x < 0.75$), and the W-rich ($x \leq 0.25$) regions. For each of these regions, the range of transition energies for each of the defect-mediated transition energies (R_1 , R_2 , B_1 , and B_2 as shown in Fig. SI 19) for each of these three classes is shown in Table SI 4. In addition, since the defect levels tend to be significantly closer to the conduction band generating shallow defect levels when the V_S defect is surrounded by W atoms, a separate range is shown by separating the range of the transition energies obtained when the V_S defect is surrounded by Mo and W atoms to emphasize the possibility of V_S defects surrounded by W atoms contributing to the PL peaks below the A exciton^{60,61} An example of this effect with the $Mo_{10}W_6S_{31}$ configurations is shown in Figure SI 21 in the supplementary data.

When the V_S defect is surrounded by W atoms, the ranges for the defect-mediated transitions match more closely to the P5 and P6 PL peaks observed in the experiment. Defect-mediated transitions associated with the d_2 and d_3 defect levels are assigned to the P5 and P6 PL peaks across the three distinct regions in Table 1 and Table SI 4. From the excitation intensity of the PL intensities of P4-P6 shown in Fig. 3e it can be seen that most of the peaks show a sublinear dependence ($k < 1$) on excitation intensity with the exception of P4 showing a superlinear ($k > 1$) dependence in region 3 (W-rich side) and P5 showing a linear dependence $k \sim 1$ in region 2 (MoW side). While the peaks do not show a clear $k \sim 1/2$ dependence, the sublinear dependence may suggest their origin

as due to free-to-bound type transitions. It is likely that in the spectral region away from the band edge the peaks may arise from both bound excitons and/or free-to-bound transitions arising from impurities/defects having energy levels within the gap of the alloyed semiconductor. Since the peaks away from the band edge should also follow the band gap increase from the Mo-rich side to the W-rich side of the $\text{Mo}_x\text{W}_{1-x}\text{S}_2$ alloyed monolayer, we can assign peak 4 (~ 1.82 eV) in region 1 and peak 3 in region 2 and 3 (~ 1.877 eV in region 2, 1.934 eV in region 3) to the same origin. The shift in the peak positions from region 1 to region 3 is ~ 114 meV. Similarly, P4 in region 2 and 3 (~ 1.835 eV in region 2, 1.871 eV in region 3) and P5 in region 3 (1.857 eV) are conjectured to be of the same origin. P6 (~ 1.6 eV) seen in all the three regions appears to be band gap independent. It should be noted that the P4-P6 peaks are not observed in the low temperature spectra from pristine monolayer WS_2 (see Fig. SI 13). Therefore, these features can be assumed to be caused by the presence of Mo in the $\text{Mo}_x\text{W}_{1-x}\text{S}_2$ alloyed monolayer.

Thus, based on the discussion above and first principles calculation of the energy levels of the most likely point defect in alloyed $\text{Mo}_x\text{W}_{1-x}\text{S}_2$, namely, V_S , the following assignments of peaks in the different regions can be made as shown in Table 1. The various radiative recombination paths of peaks 1-6 in the three regions are illustrated in Fig. 6. In the Mo-rich side peak 1 marked as B-exciton (E_B). The peaks identified with bound excitons in all the three different regions of the alloyed $\text{Mo}_x\text{W}_{1-x}\text{S}_2$ monolayer are shown with different binding energies (Δ) which are defined as the energy separation of the peak from the A-exciton peak (E_A). The free-to-bound transitions associated with V_S level, d_3 and d_2 as well with the unknown defect X are also shown in Fig. 6(a-c). The excitonic positions in monolayer of pristine MoS_2 and WS_2 are summarized in Tables SI 1-SI 2.

Table 1. Peak assignments for the alloyed monolayer $\text{Mo}_x\text{W}_{1-x}\text{S}_2$, pristine MoS_2 , and pristine WS_2 at $T=4\text{K}$.

Peak position assignment	Pristine MoS_2 (eV)	Pristine WS_2 (eV)	Mo-rich side of alloyed (eV) (Region 1)	MoW side of alloyed (eV) (Region 2)	W-rich side of alloyed (eV) (Region 3)
B-exciton	2.05	-	2.01 (P1)	-	-
A-exciton(X^0)	1.895	2.04	1.89 (P2)	1.95 (P1)	2.01 (P1)
Bound exciton $V_S^{BE}(\mathbf{d}_3)$ (associated with V_S level, \mathbf{d}_3 , Fig. 4) w/ exciton binding energy $\sim 20\text{-}36\text{ meV}^1$	1.875	2.01	1.86 (P3)	1.913 (P2)	1.975 (P2)
Bound exciton transition $V_S^{BE}(\mathbf{d}_2)$ (associated with V_S level, \mathbf{d}_2 , Fig. 4) w/ exciton binding energy $\sim 70\text{ meV}^1$	-	1.95	1.82 (P4)	1.88 (P3)	1.93 (P3)
Bound exciton/free-to-bound transition (unknown defect) (X^{BE})/(X^{FB}) w/ exciton binding energy $\sim 132 \pm 7\text{ meV}^1$	-	-	-	1.835 (P4)	1.871 (P4) 1.857 (P5)
Free-to-bound transition $V_S^{FB}(\mathbf{d}_3)$ (associated with V_S level, \mathbf{d}_3 , Fig. SI 19)	1.73	-	1.77 (P5, R2)	1.65 (P5, R2)	1.63 (P6, R2)
Free-to-bound transition $V_S^{FB}(\mathbf{d}_2)$ (associated with V_S level, \mathbf{d}_2 , Fig. SI 19)	1.68	-	1.58 (P6, R1)	1.58 (P6, R1)	-

¹ Binding energy is defined as the energy separation of the peak from the A-exciton peak ³³.

A broad band observed at $\sim 1.75\text{ eV}$ in monolayer MoS_2 similar to the P5 band in Mo-rich region of the alloyed $\text{Mo}_x\text{W}_{1-x}\text{S}_2$ monolayer in our study has been identified with an exciton bound to ionized donor levels, related to V_S ⁶². We assign the bands P5 and P6 in region 1 to a free-to-bound transition between the photoexcited electron captured at the V_S levels, \mathbf{d}_3 and \mathbf{d}_2 , respectively and a hole in the valence band. On the other hand, the peaks P3 and P4 in Mo-rich region are identified with recombination through excitons bound to V_S levels, \mathbf{d}_3 and \mathbf{d}_2 , respectively. The peaks P4 in

region 2 (MoW side) and P4 & P5 in W-rich region do not correspond to the calculated energy level positions of V_S and presumably arise from an unknown defect/impurity. It should be noted that P4 in W-rich side is considerably sharper than P5. Further P4 shows a superlinear dependence on excitation intensity ($k > 1$) in region 3 while P5 has a sublinear ($k < 1$) dependence. It may be conjectured that in region 3, P4 and P5 arise from the same defect/impurity with the former being a bound exciton and the latter being a free-to-bound transition. In intermediate MoW region, P4 may be a free-to-bound transition associated with the same defect/impurity. This defect/impurity is introduced as the W content increases.

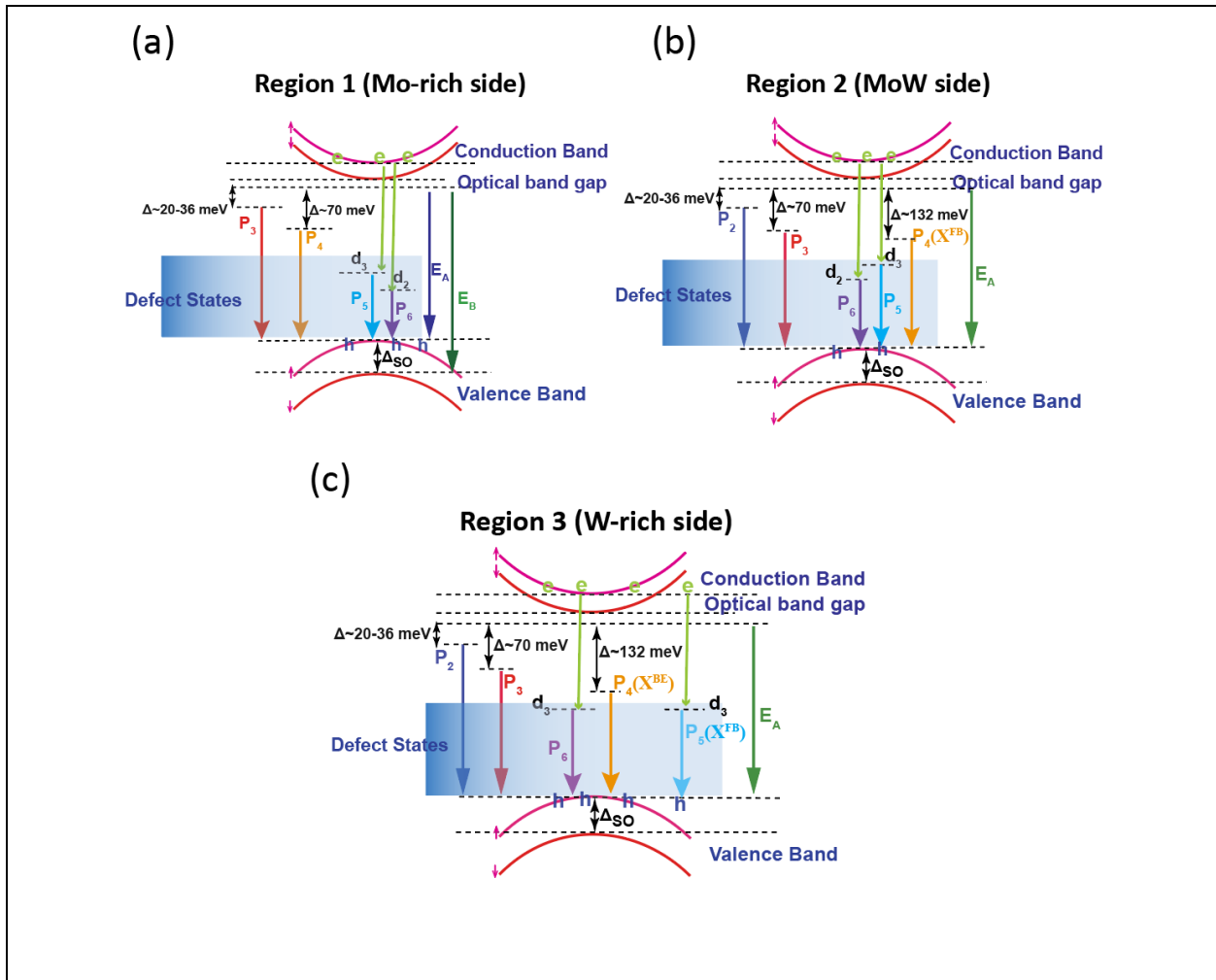


Figure 6. Various radiative recombination paths of peaks 1-6 at three regions of the alloyed $\text{Mo}_x\text{W}_{1-x}\text{S}_2$ monolayer. The energy band diagram is shown for (a) Mo-rich side, (b) intermediate

MoW side, and (c) W-rich side of the alloyed $\text{Mo}_x\text{W}_{1-x}\text{S}_2$ monolayer. The bound exciton transitions through the doublet V_S levels (d_3 , d_2) are indicated as peaks P3 & P4 in Region 1, and P2 & P3 in Regions 2 and 3. The free-to-bound transitions through d_3 and d_2 are indicated by P5 and P6 in Region 1 and Region 2. The free-to-bound transition through d_3 in Region 3 is indicated by P6. The bound exciton through the unknown defect X is indicated by P4 in Region 3. The free-to-bound transition through the defect X is indicated by P4 in Region 2 and by P5 in Region 3.

Temperature dependence of PL in alloyed $\text{Mo}_x\text{W}_{1-x}\text{S}_2$

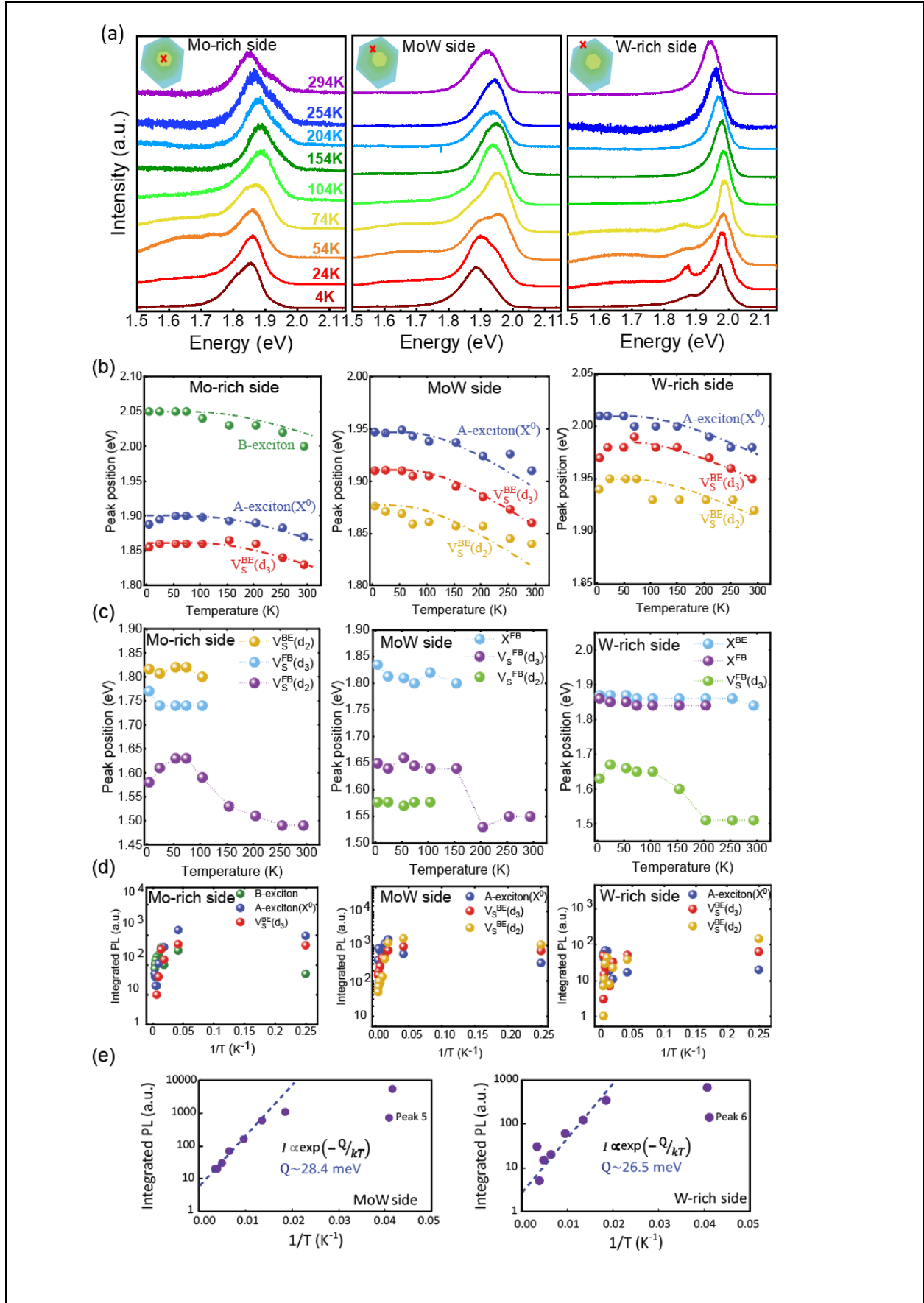


Figure 7. Evolution of PL Spectra of alloyed $\text{Mo}_x\text{W}_{1-x}\text{S}_2$ monolayer. (a) shows PL Spectra as a function of temperature for alloyed structure in region1 (Mo-rich side), region2 (intermediate MoW side), and region3 (W-rich side) of the flake. (b) Evolution of peak position with temperature for 6 peaks at the three different regions of alloyed monolayer $\text{Mo}_x\text{W}_{1-x}\text{S}_2$. Dash-dot lines are calculated with the conventional temperature dependence of semiconductor bandgap. (d) Temperature dependence of the PL intensity for the near band edge peaks for alloyed $\text{Mo}_x\text{W}_{1-x}\text{S}_2$ monolayer. (e) Temperature dependence of the PL intensity for peaks P5 and P6 from regions 2 (Intermediate MoW side) and 3 (W-rich side), respectively. Fitting an Arrhenius relation to the data yields an activation energy of 28.4 meV (P5) and 26.5 meV (P6).

To further investigate the nature of excitons and the effect of the alloy in $\text{Mo}_x\text{W}_{1-x}\text{S}_2$, temperature dependent PL spectra were taken at different regions. Figure 7(a) depicts the evolution of PL spectra for three different regions of the alloyed $\text{Mo}_x\text{W}_{1-x}\text{S}_2$ monolayer in the temperature range 4 K–300 K. (A 532 nm excitation laser was used at fixed power of 50 μW , and laser exposure time was kept at 2 sec for all spectra.) With increasing temperature, optical transition energies (peak positions) show a red shift as expected from the temperature dependence of the bandgap. The temperature dependence of the different peaks in the three regions of alloyed $\text{Mo}_x\text{W}_{1-x}\text{S}_2$ are shown in Fig. 7(b) and Fig. 7(c). We applied the O'Donnell equation⁶³ to fit the experimental peak positions near the band edge (peaks 1-3) at different temperatures (dot dash-lines in Fig. 7b) for all three regions of the alloyed monolayer $\text{Mo}_x\text{W}_{1-x}\text{S}_2$ as given by:

$$E_g(T) = E_g(0) - S \langle \hbar\omega \rangle \left[\coth \left(\frac{\langle \hbar\omega \rangle}{2kT} \right) - 1 \right] \quad (2)$$

where $E_g(0)$ is the ground-state transition energy at 0K, S is a dimensionless coupling constant and $\langle \hbar\omega \rangle$ is an average phonon energy, respectively. Table SI 3 shows the fitting parameters of peak

positions at the different regions of the alloyed monolayer $\text{Mo}_x\text{W}_{1-x}\text{S}_2$. Based on the fitting the average phonon energy $\langle \hbar\omega \rangle$ for A-exciton in pristine MoS_2 , and in Mo-rich side of the alloyed monolayer $\text{Mo}_x\text{W}_{1-x}\text{S}_2$ is 50 meV which is comparable to the reported values^{64,65}. In addition, the average phonon energy $\langle \hbar\omega \rangle$ for A-exciton (X^0) in both pristine WS_2 , and W-rich side of the alloyed monolayer $\text{Mo}_x\text{W}_{1-x}\text{S}_2$ is ~35-44 meV which is comparable to the reported values^{66,67}. Based on the Fig. 7(b) the red-shift in the peak position of B-exciton in the Mo-rich side is ~ 50 meV when the temperature increases from 4K to 300K which is comparable with reported values⁶⁸. The red shift for A-exciton in all the three regions is about ($\sim 33 \pm 3$ meV) when the temperature increases from 4K to 300K.

The peaks assigned to bound excitons associated with the V_S levels d_3 and d_2 (see Table 1) are generally stable up to room temperature with the exception of the bound exciton associated with the d_2 level in region 1 (Mo-rich side) of the alloy which disappears above 100K (Fig.7c). The peaks assigned to an unknown defect with a large exciton binding energy (132 ± 7 meV, Table 1) in regions 2 (intermediate region) and region 3 (W-rich side) persist at high temperatures, especially in W-rich region of the alloyed $\text{Mo}_x\text{W}_{1-x}\text{S}_2$ monolayer (Fig.7c). The radiative transitions assigned to free-to-bound transitions involving V_S levels d_3 ($V_S^{\text{FB}}(d_3)$) are present even at room temperature. (See Fig. SI 8 for a comparison of the PL spectra at low and high temperatures from the three regions). Interestingly, $V_S^{\text{FB}}(d_3)$ and $V_S^{\text{FB}}(d_2)$ transitions, are very prominent at low temperature in pristine MoS_2 (see Fig. SI 12) and persist as a broad tail on the low energy side of the band excitons even at high temperatures. This observation suggests that the V_S levels dominate the radiative process in pristine MoS_2 especially at low temperatures. While the free-to-bound transitions via V_S levels dominate in pristine MoS_2 , the bound excitons associated with V_S levels

are observed in pristine WS₂ in the temperature range 4-304 K (see Fig. SI 13). Thus, V_S plays an important role in the radiative processes in both MoS₂ and WS₂ as well as in the alloyed monolayer Mo_xW_{1-x}S₂. The dominance of either the free-to-bound transitions or the bound exciton transitions involving the V_S levels will be determined by the relative radiative rates of the transitions and the thermal ionization of the photoexcited electron from the V_S level, especially at high temperatures, which may differ between MoS₂ and WS₂ layers.

Figure 7(d) shows the integrated PL intensity versus reciprocal of temperature for near the band edge (peaks 1-3) in all the three regions of alloyed monolayer Mo_xW_{1-x}S₂. The PL intensity (I_{PL}) decreases at high temperatures suggesting an Arrhenius type behavior^{69, 10}. The quenching of the free-to-bound transitions via the d₃ level of V_S (P5 in region 2 and P6 in region 3, Table 1) is shown Fig. 7(e). Fitting an Arrhenius relation $I_{PL} = const * e^{\frac{Q}{kT}}$ to the data gives an activation energy Q ~ 26-28 meV. This value perhaps suggests the thermalization energy of the photoexcited electron captured at the d₃ level of V_S. A comparable activation energy of ~ 36 meV was reported for PL emission associated with V_S in monolayer WS₂ and was attributed to the thermal dissociation of the bound exciton³³.

Figure SI 3 shows the FWHM versus temperature for the near band edge peaks (peaks 1-3) in the three regions of the alloyed Mo_xW_{1-x}S₂. It can be seen that the temperature dependence of FWHM could not be fitted to the equation describing the electron-phonon interaction (EQ (1) in SI). The A-exciton peak is broader in regions 1 and 2 in comparison to region 3. The FWHM of the peaks associated with bound exciton transitions involving V_S levels are in the range 60-80 meV. Compared to the pristine WS₂ and MoS₂, the changes of the FWHM for A-exciton (X⁰) in region 1 and region 2 of the monolayer Mo_xW_{1-x}S₂ is larger than the changes of FWHM for pristine samples. For region 1 (Mo-rich side) of the alloy it changes from 70 meV to 120 meV upon

increasing the temperature from 4 K to 300 K. However, for the pristine MoS₂ FWHM of the A-exciton changes from 38 meV to 50 meV (Fig. SI 15). For the region 3 (W-rich side) of the alloy it changes from 38 meV to 45 meV upon increasing the temperature from 4 K to 300 K (Fig. SI 3). For pristine WS₂, the FWHM changes from 45 meV to 52meV (Fig. SI15) which is larger than the reported values for pristine MoS₂⁷⁰, and pristine WS₂⁶⁷.

CONCLUSION

In summary, using an alkali metal halide-assisted chemical vapor deposition approach, we successfully synthesized triangular TMDC alloy (Mo_xW_{1-x}S₂) monolayers with continuously varied W/Mo concentration from the center to edges. The combined experimental photoluminescence characterization with theoretical DFT calculations including spin-orbit interactions enabled thorough investigation of the nature of myriad intralayer optical transitions excitons in the alloyed monolayers. Aberration-corrected high-angle annular dark-field scanning transmission electron microscopy showed the presence of sulfur monovacancy, V_S, whose concentration varied across the graded Mo_xW_{1-x}S₂ layer as a function of Mo content with the highest value in the Mo rich center region. We identified free-to-bound transitions involving a photoexcited electron captured at the doublet V_S level and a hole in the top of the valence band by matching the calculated spin-allowed optical transition energies through a doublet V_S level in the gap. In addition, two bound exciton transitions associated with the V_S doublet were also identified. Further, the study of the temperature dependence of the photoluminescence helped to identify the differences brought about by alloying in comparison to the pure MoS₂ and WS₂ monolayers. Thus, a plethora of V_S related intralayer optical transitions reported for the first time in the alloy Mo_xW_{1-x}S₂, reveals the interplay between composition and defect structure. Our work highlights the

capability of modulating the bandgap and engineering the defect structures simultaneously in 2D graded TMDC alloys via controllable synthesis strategies, and systematically studies how the optical transitions are modulated by the presence of structural defects.

MATERIALS AND METHODS

The Growth of Monolayer $\text{Mo}_x\text{W}_{1-x}\text{S}_2$ alloys. To grow alloyed $\text{Mo}_x\text{W}_{1-x}\text{S}_2$ monolayers, powders of MoS_2 (~5 mg), WO_3 (~5 mg), and NaBr (~0.5 mg) were mixed uniformly and placed inside a porcelain boat, and a piece of clean SiO_2/Si was placed on top of the boat with the polished side facing down. Note that the use of NaBr promoter can enhance the coverage of monolayers and increase the reproducibility of alloys. Subsequently, this porcelain boat was loaded into a one-inch quartz tube for the CVD growth, and another porcelain boat containing sulfur powders (300 mg) was loaded upstream. In the growth process, the mixed $\text{MoS}_2/\text{WO}_3/\text{NaBr}$ powders and the substrate were heated up to 825 °C and held for 10 min, and sulfur powders were heated up to 220 °C simultaneously for evaporation. Argon gas (100 sccm) was used as the carrier gas throughout the growth process.

AC-HAADF-STEM. High-resolution aberration controlled HAADF-STEM images were taken using a FEI Titan3 G2 S/TEM operated at 80 kV and equipped with double spherical aberration correction and monochromator. Images were acquired using a HAADF detector with a collection angle of 42-244 mrad, camera height of 115 mm, convergence angle of 30 rad, and a beam current of 50 pA. For the identification of sulfur mono-vacancies, AC-HRSTEM images were Fourier filtered using a low pass filter in the Digital Micrograph suite. In the same software, integrated

intensity line scans were taken along the armchair direction and the relative intensity of two overlapped sulfur atoms was used as a reference to identify sulfur mono-vacancies.

Optical Measurements. The power and temperature-dependent PL spectra were measured by the confocal laser scanning microscope system equipped with a vibration-free closed-cycle cryostat (Attodry 800, attocube). A 532 nm CW laser as an excitation source was focused into a small spot with a diameter of approximately 2-3 μm on the sample through a 100 \times objective lens (APO/VIS, N.A. = 0.82; attocube) inside the vacuum chamber. The PL spectra was then collected by the same lens and filtered the excitation signal by a 532 nm long-pass filter before entering a spectrometer (Andor) which consisted of a monochromator and a thermoelectrically cooled CCD camera. Room temperature hyperspectral PL was collected using AFM assisted diffraction limited PL (neaspac co.) recorded using a 328 mm focal length Andor spectrometer and imaged with a liquid nitrogen cooled silicon EMCCD camera (Andor iXon).

DFT Calculation. We have performed theoretical calculations using Quantum Espresso (QE)⁷¹ to aid in the interpretation of experimental results. The alloys are modeled using a hexagonal unit cell consisting of 3 atoms (either MoS₂ or WS₂) and are expanded to create a 4 x 4 x 1 supercell consisting of 48 atoms with stoichiometry Mo_{0.16x}W_{0.16(1-x)}S₃₂ and varying Mo concentration (x). All calculations are performed using norm-conserving PBE⁷² pseudopotentials⁷³ with the spin-orbit coupling (SOC) interaction included⁷⁴. The lattice constant is set to $a = (3.183 - 0.002x)$ Å, which is based on the relaxed lattice constants of 3.181 Å for MoS₂ and 3.183 Å for WS₂. The force convergence threshold is set to 0.01 eV/Å, while the total energy threshold is set to 10⁻⁶ eV. Also, calculations are performed using a 2 x 2 x 1 k-point mesh and the kinetic energy cutoff is 680 eV. The cell parameter in the z-direction is set to $c = 14.2$ Å to introduce a vacuum region and

prevent undesired interactions between the monolayers. All possible alloy structures are constructed by substituting Mo and W atoms at the transition metal sites while preserving the C_{3v} symmetry. Assuming symmetry preservation, 32 possible alloyed structures can be generated in the $4 \times 4 \times 1$ supercell and the band structures for all 32 structures are determined both with and without a single V_s introduced (Fig. SI 18). All band structures are calculated using a Γ -M-K- Γ k-point path with the z-directional electronic spinor $\langle S_z \rangle$ also calculated to distinguish between spin up (blue) and down (red) states. From the calculated band structures, the various transitions at the K point are investigated to determine how the Mo concentration and geometry of the configuration affect these transitions.

ACKNOWLEDGMENTS

M.G. and Y.A. acknowledge support from Air Force Office of Scientific Research (AFOSR) grant number FA9550-19-0252 and FA9550-23-1-0375. T.Z., D.Z., D.H. and M.T. acknowledge support from the AFOSR through grant No. FA9550-18-1-0072 and the NSF-IUCRC Center for Atomically Thin Multifunctional Coatings (ATOMIC). H.T. and Z.D.W. acknowledge funding support from the USA National Science Foundation (Award 2013640) and are grateful to the “Advanced Cyberinfrastructure Coordination Ecosystem: Services & Support” (ACCESS), which is supported by National Science Foundation grant number ACI-1548562 through proposal TG-DMR170008.

Author Contribution

Y.A. and M.G. conceived the project. M.G. carried out the power and temperature-dependent PL experiments. T.Z., D.Z., and D.S. grew the samples and AC-HRSTEM measurements. M.G., and

V.S. analyzed the experimental data. Z.D.W, and H.T. performed the DFT calculations. All authors discussed the results and contributed to writing the manuscript. Y.A. supervised the overall project.

Competing interests

The authors declare no competing interests.

Materials & Correspondence

All correspondence and material requests should be addressed to yohannes.abate@uga.edu.

REFERENCES

- 1 Chaves, A. *et al.* Bandgap engineering of two-dimensional semiconductor materials. *npj 2D Materials and Applications* **4** (2020). <https://doi.org:10.1038/s41699-020-00162-4>
- 2 Lei, Y. *et al.* Graphene and Beyond: Recent Advances in Two-Dimensional Materials Synthesis, Properties, and Devices. *ACS Nanoscience Au* **2**, 450-485 (2022). <https://doi.org:10.1021/acsnanoscienceau.2c00017>
- 3 Novoselov, K. S. *et al.* Electric field effect in atomically thin carbon films. *science* **306**, 666-669 (2004).
- 4 Roy, S. *et al.* Structure, Properties and Applications of Two-Dimensional Hexagonal Boron Nitride. *Advanced Materials* **33**, 2101589 (2021).
- 5 Ghafariasl, M. *et al.* Photodegradation and Thermal Effects in Violet Phosphorus. arXiv:2307.03814 (2023). <<https://ui.adsabs.harvard.edu/abs/2023arXiv230703814G>>.
- 6 Yin, X. *et al.* Recent developments in 2D transition metal dichalcogenides: phase transition and applications of the (quasi-) metallic phases. *Chemical Society Reviews* (2021).
- 7 Meng, D. *et al.* Electronic structure and dynamic properties of two-dimensional $W_xMo_{1-x}S_2$ ternary alloys from first-principles calculations. *Computational Materials Science* **182**, 109797 (2020).
- 8 Zheng, S. *et al.* Monolayers of $W_xMo_{1-x}S_2$ alloy heterostructure with in-plane composition variations. *Applied Physics Letters* **106**, 063113 (2015). <https://doi.org:10.1063/1.4908256>
- 9 Chen, Y. *et al.* Temperature-dependent photoluminescence emission and Raman scattering from $Mo_{1-x}W_xS_2$ monolayers. *Nanotechnology* **27**, 445705 (2016). <https://doi.org:10.1088/0957-4484/27/44/445705>

- 10 Li, H. & Zhang, X. Temperature-dependent photoluminescence and time-resolved photoluminescence study of monolayer molybdenum disulfide. *Optical Materials* **107**, 110150 (2020).
- 11 Sharma, S., Bhagat, S., Singh, J., Ahmad, M. & Sharma, S. Temperature dependent photoluminescence from WS₂ nanostructures. *Journal of Materials Science: Materials in Electronics* **29**, 20064-20070 (2018). <https://doi.org:10.1007/s10854-018-0137-3>
- 12 Conley, H. J. *et al.* Bandgap engineering of strained monolayer and bilayer MoS₂. *Nano letters* **13**, 3626-3630 (2013).
- 13 Wang, F. *et al.* Strain engineering in monolayer WS₂ and WS₂ nanocomposites. *2D Materials* **7**, 045022 (2020).
- 14 Kang, J., Tongay, S., Li, J. & Wu, J. Monolayer semiconducting transition metal dichalcogenide alloys: Stability and band bowing. *Journal of Applied Physics* **113**, 143703 (2013).
- 15 Tan, W. *et al.* Ordered and disordered phases in Mo_{1-x}W_xS₂ monolayer. *Scientific reports* **7**, 1-8 (2017).
- 16 Susarla, S. *et al.* Quaternary 2D Transition Metal Dichalcogenides (TMDs) with Tunable Bandgap. *Adv Mater* **29** (2017). <https://doi.org:10.1002/adma.201702457>
- 17 Kang, H. S. *et al.* Bowing-alleviated continuous bandgap engineering of wafer-scale WS₂xSe₂(1-x) monolayer alloys and their assembly into hetero-multilayers. *NPG Asia Materials* **14** (2022). <https://doi.org:10.1038/s41427-022-00437-w>
- 18 Li, H. *et al.* Growth of alloy MoS(2x)Se₂(1-x) nanosheets with fully tunable chemical compositions and optical properties. *J Am Chem Soc* **136**, 3756-3759 (2014). <https://doi.org:10.1021/ja500069b>
- 19 Gong, Y. *et al.* Band gap engineering and layer-by-layer mapping of selenium-doped molybdenum disulfide. *Nano Lett* **14**, 442-449 (2014). <https://doi.org:10.1021/nl4032296>
- 20 Xie, L. M. Two-dimensional transition metal dichalcogenide alloys: preparation, characterization and applications. *Nanoscale* **7**, 18392-18401 (2015). <https://doi.org:10.1039/c5nr05712d>
- 21 Feng, Q. *et al.* Growth of MoS₂ (1-x) Se₂ x (x= 0.41–1.00) monolayer alloys with controlled morphology by physical vapor deposition. *ACS nano* **9**, 7450-7455 (2015).
- 22 Chen, Y. *et al.* Tunable band gap photoluminescence from atomically thin transition-metal dichalcogenide alloys. *Acs Nano* **7**, 4610-4616 (2013).
- 23 Jiang, J. *et al.* Synergistic additive-mediated CVD growth and chemical modification of 2D materials. *Chemical Society Reviews* **48**, 4639-4654 (2019).
- 24 Lee, Y. H. *et al.* Synthesis of large-area MoS₂ atomic layers with chemical vapor deposition. *Advanced materials* **24**, 2320-2325 (2012).
- 25 Zhou, J. *et al.* A library of atomically thin metal chalcogenides. *Nature* **556**, 355-359 (2018).
- 26 Zhang, T., Voshell, A., Zhou, D., Ward, Z.D., Yu, Z., Liu, M., Aponte, K.O.D., Granzier-Nakajima, T., Lei, Y., Liu, H. and Terrones, H., . Effects of post-transfer annealing and substrate interactions on the photoluminescence of 2D/3D monolayer WS₂/Ge heterostructures. *Nanoscale* (2023). <https://doi.org:10.1039/d3nr00961k> From NLM Publisher.
- 27 Zhang, T. *et al.* Universal in situ substitutional doping of transition metal dichalcogenides by liquid-phase precursor-assisted synthesis. *ACS nano* **14**, 4326-4335 (2020).

- 28 Fali, A. *et al.* Photodegradation Protection in 2D In-Plane Heterostructures Revealed by Hyperspectral Nanoimaging: The Role of Nanointerface 2D Alloys. *ACS Nano* **15**, 2447-2457 (2021). <https://doi.org:10.1021/acsnano.0c06148>
- 29 Bogaert, K. *et al.* Two-dimensional MoxW1- xS2 graded alloys: growth and optical properties. *Scientific reports* **8**, 1-7 (2018).
- 30 Lin, Z. *et al.* Facile synthesis of MoS2 and MoxW1-xS2 triangular monolayers. *Appl Materials* **2**, 092514 (2014).
- 31 Azizi, A. *et al.* Spontaneous formation of atomically thin stripes in transition metal dichalcogenide monolayers. *Nano letters* **16**, 6982-6987 (2016).
- 32 Hong, J. *et al.* Exploring atomic defects in molybdenum disulphide monolayers. *Nature communications* **6**, 6293 (2015).
- 33 Carozo, V. *et al.* Optical identification of sulfur vacancies: Bound excitons at the edges of monolayer tungsten disulfide. *Science advances* **3**, e1602813 (2017).
- 34 Lee, C.-S. *et al.* Programmed band gap modulation within van der Waals semiconductor monolayers by metalorganic vapor-phase epitaxy. *Chemistry of Materials* **32**, 5084-5090 (2020).
- 35 Hill, R. Energy-gap variations in semiconductor alloys. *Journal of Physics C: Solid State Physics* **7**, 521 (1974).
- 36 Gupta, G., Kallatt, S. & Majumdar, K. Direct observation of giant binding energy modulation of exciton complexes in monolayer MoS e 2. *Physical Review B* **96**, 081403 (2017).
- 37 Chernikov, A., Ruppert, C., Hill, H. M., Rigosi, A. F. & Heinz, T. F. Population inversion and giant bandgap renormalization in atomically thin WS2 layers. *Nature Photonics* **9**, 466-470 (2015). <https://doi.org:10.1038/nphoton.2015.104>
- 38 Mak, K. F. *et al.* Tightly bound trions in monolayer MoS2. *Nature materials* **12**, 207-211 (2013).
- 39 Steinhoff, A., Rosner, M., Jahnke, F., Wehling, T. O. & Gies, C. Influence of excited carriers on the optical and electronic properties of MoS2. *Nano letters* **14**, 3743-3748 (2014).
- 40 Peimyoo, N. *et al.* Thermal conductivity determination of suspended mono- and bilayer WS2 by Raman spectroscopy. *Nano Research* **8**, 1210-1221 (2014). <https://doi.org:10.1007/s12274-014-0602-0>
- 41 Schmidt, T., Lischka, K. & Zulehner, W. Excitation-power dependence of the near-band-edge photoluminescence of semiconductors. *Physical Review B* **45**, 8989 (1992).
- 42 Kaplan, D. *et al.* Excitation intensity dependence of photoluminescence from monolayers of MoS2 and WS2/MoS2 heterostructures. *2D Materials* **3**, 015005 (2016). <https://doi.org:10.1088/2053-1583/3/1/015005>
- 43 Zhao, W. *et al.* Evolution of electronic structure in atomically thin sheets of WS2 and WSe2. *ACS nano* **7**, 791-797 (2013).
- 44 Hill, H. M. *et al.* Observation of Excitonic Rydberg States in Monolayer MoS2 and WS2 by Photoluminescence Excitation Spectroscopy. *Nano Lett* **15**, 2992-2997 (2015). <https://doi.org:10.1021/nl504868p>
- 45 Cong, C., Shang, J., Wang, Y. & Yu, T. Optical properties of 2D semiconductor WS2. *Advanced Optical Materials* **6**, 1700767 (2018).

- 46 Kylanpää, I. & Komsa, H.-P. Binding energies of exciton complexes in transition metal dichalcogenide monolayers and effect of dielectric environment. *Physical Review B* **92**, 205418 (2015). <https://doi.org/10.1103/PhysRevB.92.205418>
- 47 Danovich, M., Zólyomi, V., Fal'ko, V. I. & Aleiner, I. L. Auger recombination of dark excitons in WS₂ and WSe₂ monolayers. *2D Materials* **3**, 035011 (2016).
- 48 Kahnouji, H., Kratzer, P. & Hashemifar, S. J. Ab initio simulation of the structure and transport properties of zirconium and ferromagnetic cobalt contacts on the two-dimensional semiconductor WS₂. *Physical Review B* **99**, 035418 (2019).
- 49 Kormányos, A., Zólyomi, V., Drummond, N. D. & Burkard, G. Spin-orbit coupling, quantum dots, and qubits in monolayer transition metal dichalcogenides. *Physical Review X* **4**, 011034 (2014).
- 50 Zhong, M. *et al.* Electronic structure and exciton shifts in Sb-doped MoS₂ monolayer. *npj 2D Materials and Applications* **3**, 1 (2019).
- 51 Guo, S.-D. Spin-orbit and strain effect on power factor in monolayer MoS₂. *Computational Materials Science* **123**, 8-13 (2016).
- 52 Li, Z., Wang, T., Miao, S., Lian, Z. & Shi, S.-F. Fine structures of valley-polarized excitonic states in monolayer transitional metal dichalcogenides. *Nanophotonics* **9**, 1811-1829 (2020).
- 53 Kim, J. G., Yun, W. S., Jo, S., Lee, J. & Cho, C.-H. Effect of interlayer interactions on exciton luminescence in atomic-layered MoS₂ crystals. *Scientific reports* **6**, 1-7 (2016).
- 54 Wang, Y. *et al.* Spin-valley locking effect in defect states of monolayer MoS₂. *Nano Letters* **20**, 2129-2136 (2020).
- 55 Tan, A. M. Z., Freysoldt, C. & Hennig, R. G. Stability of charged sulfur vacancies in 2D and bulk MoS₂ from plane-wave density functional theory with electrostatic corrections. *Physical Review Materials* **4**, 064004 (2020).
- 56 Schuler, B. *et al.* Large spin-orbit splitting of deep in-gap defect states of engineered sulfur vacancies in monolayer WS₂. *Physical review letters* **123**, 076801 (2019).
- 57 Wu, K. *et al.* Revealing the Competition between Defect-Trapped Exciton and Band-Edge Exciton Photoluminescence in Monolayer Hexagonal WS₂. *Advanced Optical Materials* **10**, 2101971 (2022).
- 58 Li, Z. *et al.* Active light control of the MoS₂ monolayer exciton binding energy. *ACS nano* **9**, 10158-10164 (2015).
- 59 Zhu, B., Chen, X. & Cui, X. Exciton binding energy of monolayer WS₂. *Scientific reports* **5**, 1-5 (2015).
- 60 Haneef, H. F., Zeidell, A. M. & Jurchescu, O. D. Charge carrier traps in organic semiconductors: A review on the underlying physics and impact on electronic devices. *Journal of Materials Chemistry C* **8**, 759-787 (2020).
- 61 Reshchikov, M. A., Morkoç, H., Park, S. & Lee, K. Transient photoluminescence of defect transitions in freestanding GaN. *Applied Physics Letters* **78**, 2882-2884 (2001).
- 62 Greben, K., Arora, S., Harats, M. G. & Bolotin, K. I. Intrinsic and extrinsic defect-related excitons in TMDCs. *Nano Letters* **20**, 2544-2550 (2020).
- 63 O'donnell, K. & Chen, X. Temperature dependence of semiconductor band gaps. *Applied physics letters* **58**, 2924-2926 (1991).

- 64 Saigal, N. & Ghosh, S. Evidence for two distinct defect related luminescence features in monolayer MoS₂. *Applied Physics Letters* **109** (2016). <https://doi.org:10.1063/1.4963133>
- 65 Pandey, J. & Soni, A. Unraveling biexciton and excitonic excited states from defect bound states in monolayer MoS₂. *Applied Surface Science* **463**, 52-57 (2019). <https://doi.org:10.1016/j.apsusc.2018.08.205>
- 66 Wei, K., Liu, Y., Yang, H., Cheng, X. & Jiang, T. Large range modification of exciton species in monolayer WS₂. *Appl Opt* **55**, 6251-6255 (2016). <https://doi.org:10.1364/AO.55.006251>
- 67 Krustok, J. *et al.* Local strain-induced band gap fluctuations and exciton localization in aged WS₂ monolayers. *AIP Advances* **7** (2017). <https://doi.org:10.1063/1.4985299>
- 68 Sharma, R. *et al.* Spectroscopic correlation of chalcogen defects in atomically thin MoS₂(1-x)Se_{2x} alloys. *Journal of Physics: Materials* **3** (2020). <https://doi.org:10.1088/2515-7639/abab6a>
- 69 Saigal, N. & Ghosh, S. Evidence for two distinct defect related luminescence features in monolayer MoS₂. *Applied Physics Letters* **109**, 122105 (2016).
- 70 Cadiz, F. *et al.* Excitonic linewidth approaching the homogeneous limit in MoS₂-based van der Waals heterostructures. *Physical Review X* **7**, 021026 (2017).
- 71 Giannozzi, P. *et al.* QUANTUM ESPRESSO: a modular and open-source software project for quantum simulations of materials. *Journal of physics: Condensed matter* **21**, 395502 (2009).
- 72 Perdew, J. P., Burke, K. & Ernzerhof, M. Generalized gradient approximation made simple. *Physical review letters* **77**, 3865 (1996).
- 73 Hamann, D. Optimized norm-conserving Vanderbilt pseudopotentials. *Physical Review B* **88**, 085117 (2013).
- 74 Dal Corso, A. & Conte, A. M. Spin-orbit coupling with ultrasoft pseudopotentials: Application to Au and Pt. *Physical Review B* **71**, 115106 (2005).

Supplementary data

Sulfur Vacancy Related Optical Transitions in Graded Alloys of $\text{Mo}_x\text{W}_{1-x}\text{S}_2$ Monolayers

Mahdi Ghafariasl¹, Tianyi Zhang², Zachary D. Ward³, Da Zhou⁴, David Sanchez²,
Venkataraman Swaminathan⁵, Humberto Terrones³, Mauricio Terrones^{2,4,6}, Yohannes Abate^{1*}

¹ Department of Physics and Astronomy, University of Georgia, Athens, Georgia 30602, USA

² Department of Materials Science and Engineering, The Pennsylvania State University,
University Park, PA 16802, USA

³ Department of Physics and Astronomy, Rensselaer Polytechnic Institute, Rensselaer, New York
12180, USA

⁴ Department of Physics, The Pennsylvania State University, University Park, PA 16802, USA

⁵ Department of Materials Science and Nanoengineering Rice University Houston, TX 77005,
USA

⁶ Department of Chemistry, The Pennsylvania State University, University Park, PA 16802,
USA

*Corresponding author E-mail: yohannes.abate@uga.edu

PL spectra at 4K and fitting parameters at different regions of alloyed $\text{Mo}_x\text{W}_{1-x}\text{S}_2$ monolayer

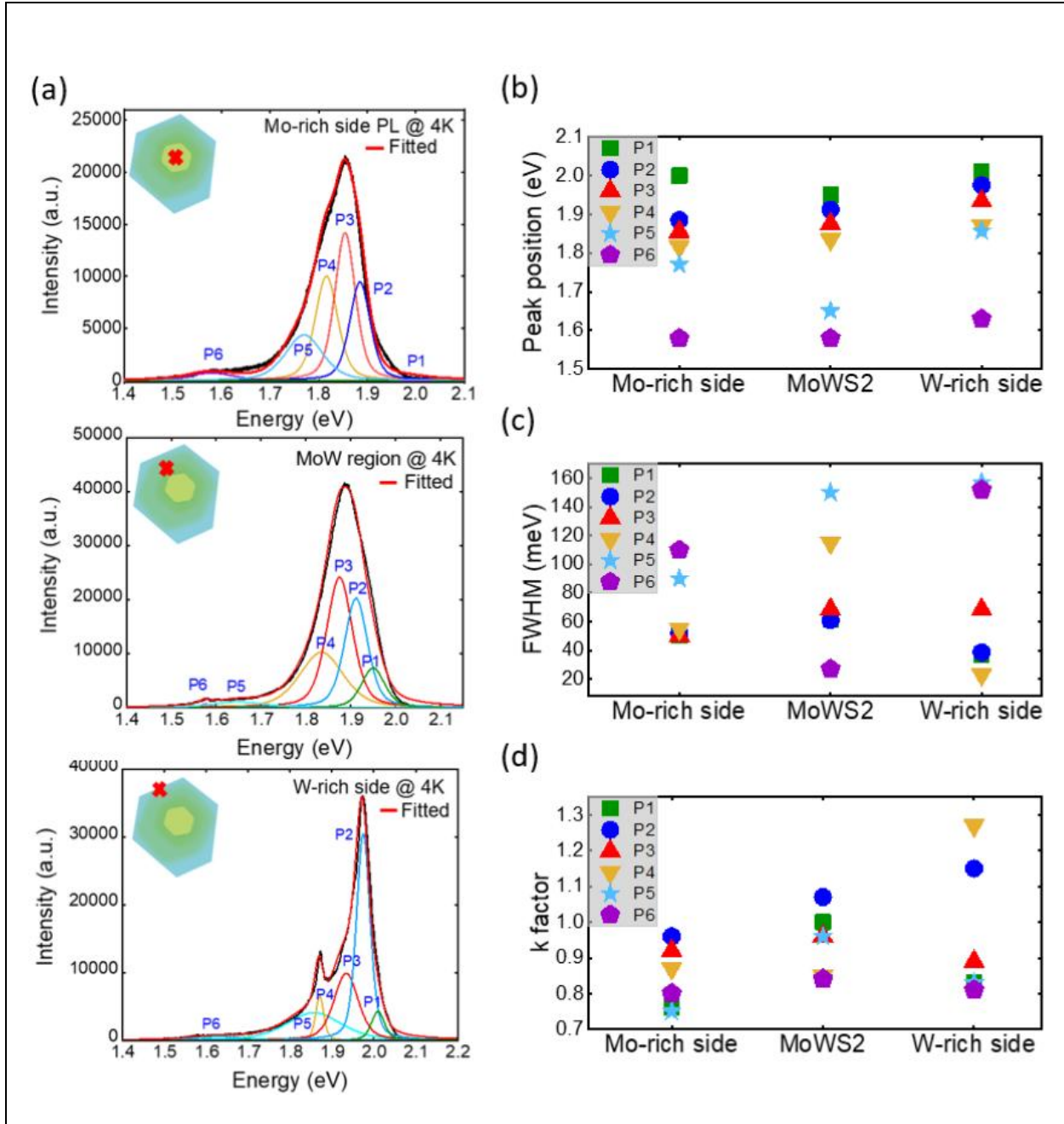


Figure SI 1. PL spectra at 4K and fitting parameters at different regions of alloyed monolayer $\text{Mo}_x\text{W}_{1-x}\text{S}_2$. (a) Peaks P1-P6 represent the pseudo-Voigt fits in three different regions of the

alloyed monolayer $\text{Mo}_x\text{W}_{1-x}\text{S}_2$; Mo-rich region (center), an intermediate region, and W-rich region (edge), respectively. (b) Comparison of the peak positions in the different regions. (c) Comparison of FWHM of the different spectral peaks in the three regions. (d) Comparison of the k factor from the excitation dependence of PL intensity of the different spectral peaks in the various regions. See the main article for the discussion on the k factor. For PL spectra the power is $100 \mu\text{W}$ and the temperature of 4K.

The comparison of the A-exciton peak positions in the Mo-rich region (P2), the intermediate region (P1), and the W-rich region (P1), shows that the band edge PL peaks shift monotonically to higher energy from center to edge consistent with the center being Mo-rich and the edge being W-rich (Fig. SI 1 (b)). Figure SI 1(c) shows the comparison of the FWHM of different spectral peaks (P1-P6) in different regions of the alloyed structure. In general, peaks P4-P6 are broader ($\geq 100 \text{ meV}$) than the band edge transitions P1-P3 ($\leq 60 \text{ meV}$) and the latter are narrower at the edge (W-rich) than at the center (Mo-rich). Peak 4 on the W-rich side which is attributed to a bound exciton due to an unknown defect/impurity shows the narrowest linewidth. (See Table 1 in the main article for the peak assignments). The k-factors for the excitation dependence of PL intensity of the different spectral peaks are plotted in Fig. SI 1(d) and the assignments of the peaks based on their values are discussed in the main article.

Power dependence of FWHM for alloyed monolayer $\text{Mo}_x\text{W}_{1-x}\text{S}_2$

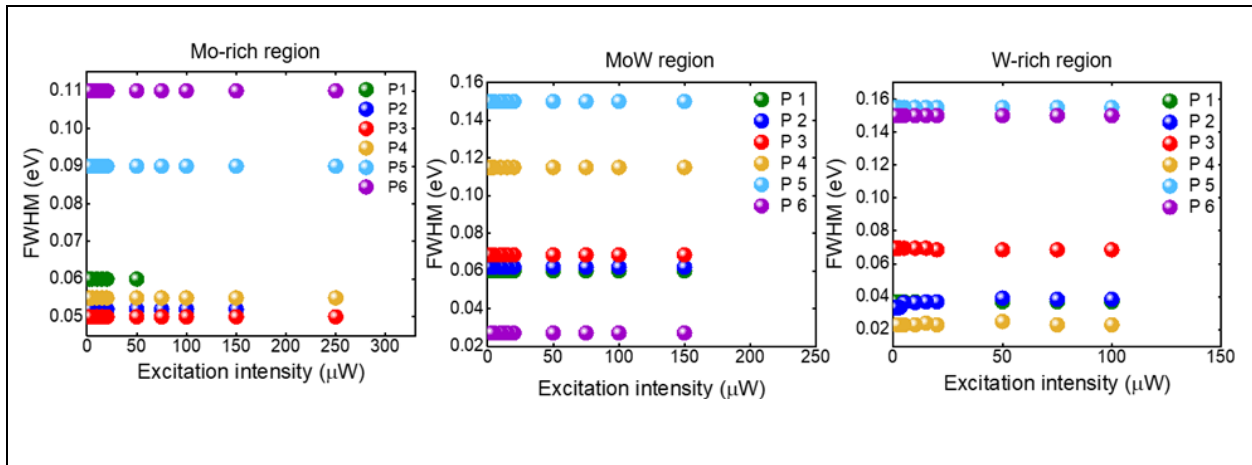


Figure SI 2. Power dependence of FWHM for the six peaks at three different regions of alloyed monolayer $\text{Mo}_x\text{W}_{1-x}\text{S}_2$ showing negligible effect.

Temperature dependence of FWHM for alloyed monolayer $\text{Mo}_x\text{W}_{1-x}\text{S}_2$

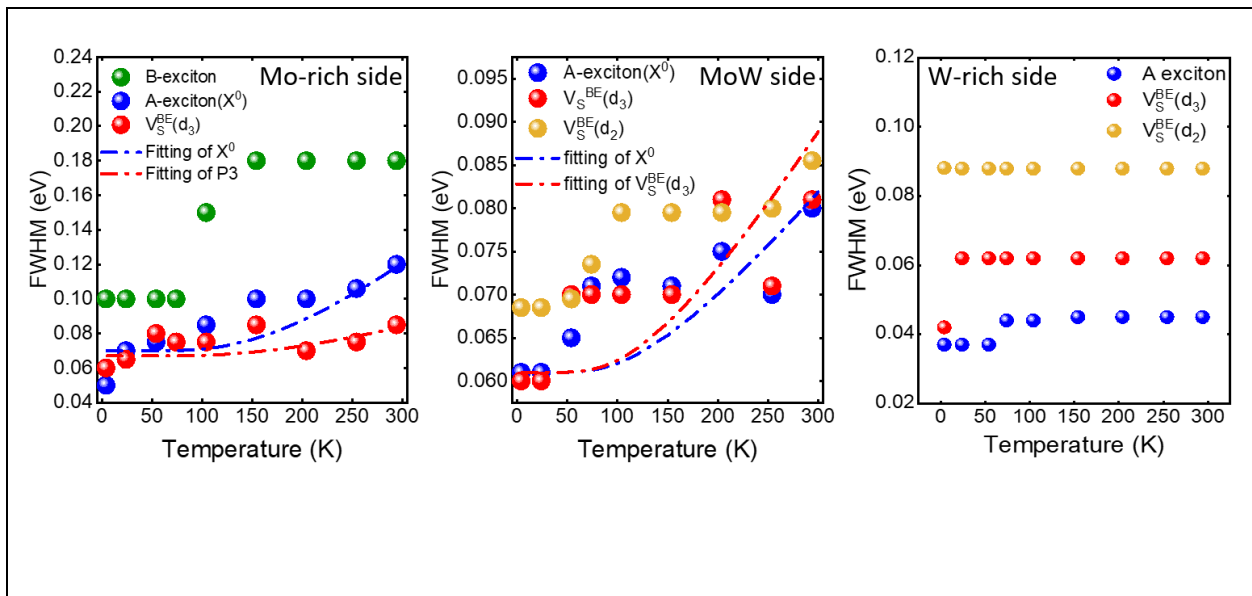


Figure SI 3. Temperature dependence of FWHM for alloyed monolayer $\text{Mo}_x\text{W}_{1-x}\text{S}_2$

The linewidth of the exciton transition as a function of temperature in TMDCs has been explained in terms electron-phonon interactions as given by the following equation ^{1,2}

$$\gamma = \gamma_I + \frac{b}{\exp\left(\frac{\Theta}{KT}\right) - 1} \quad (1)$$

Where γ_I is the temperature independent inhomogeneous broadening, Θ is either a dominant phonon or an average phonon energy. The above equation appears to be a reasonable description of the temperature dependence of the linewidth of the A exciton in pristine MoS₂ and WS₂ as shown in Fig. SI 15. However, Fig. SI 3 clearly shows that the FWHM versus temperature data in the alloyed Mo_xW_{1-x}S₂ cannot be fitted to the above equation. Presumably, in the alloyed semiconductor, the use of an average phonon energy is not an adequate representation of the electron-phonon interactions. Perhaps both acoustic as well as optical phonon interactions have to be taken into account with the former dominating at low to intermediate temperature range and the latter at high temperatures³.

Temperature dependence of intensity for alloyed monolayer Mo_xW_{1-x}S₂

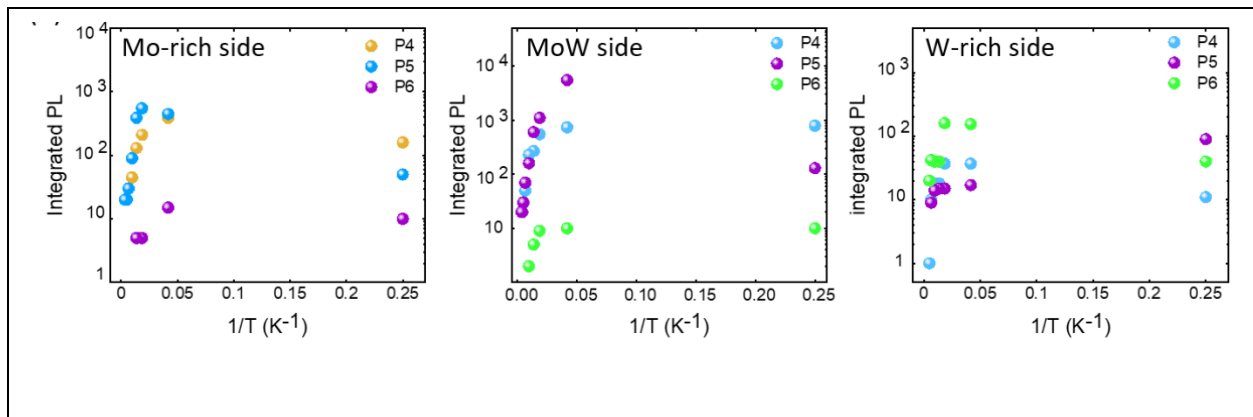


Figure SI 4. Temperature dependence of intensity for far from the band edge peaks (peaks 4-6) of alloyed monolayer Mo_xW_{1-x}S₂.

Temperature dependence of PL from different regions of alloyed monolayer $\text{Mo}_x\text{W}_{1-x}\text{S}_2$

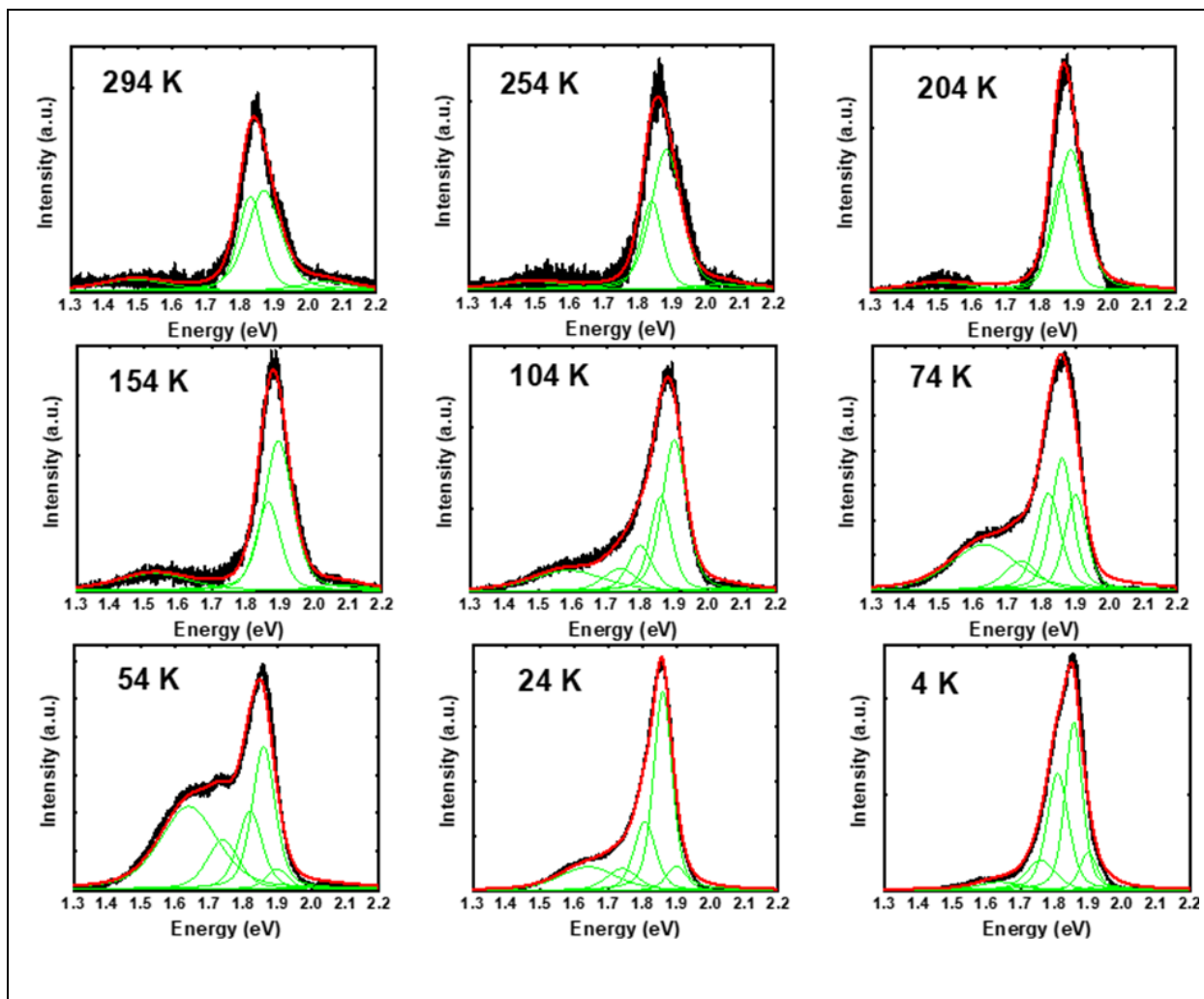


Figure SI 5. PL spectra from Mo-rich side of alloyed $\text{Mo}_x\text{W}_{1-x}\text{S}_2$ at different temperatures ranging from 4 K to 300 K. The spectra are deconvoluted with six pseudo-Voigt peaks below 104 K and four peaks above 104 K.

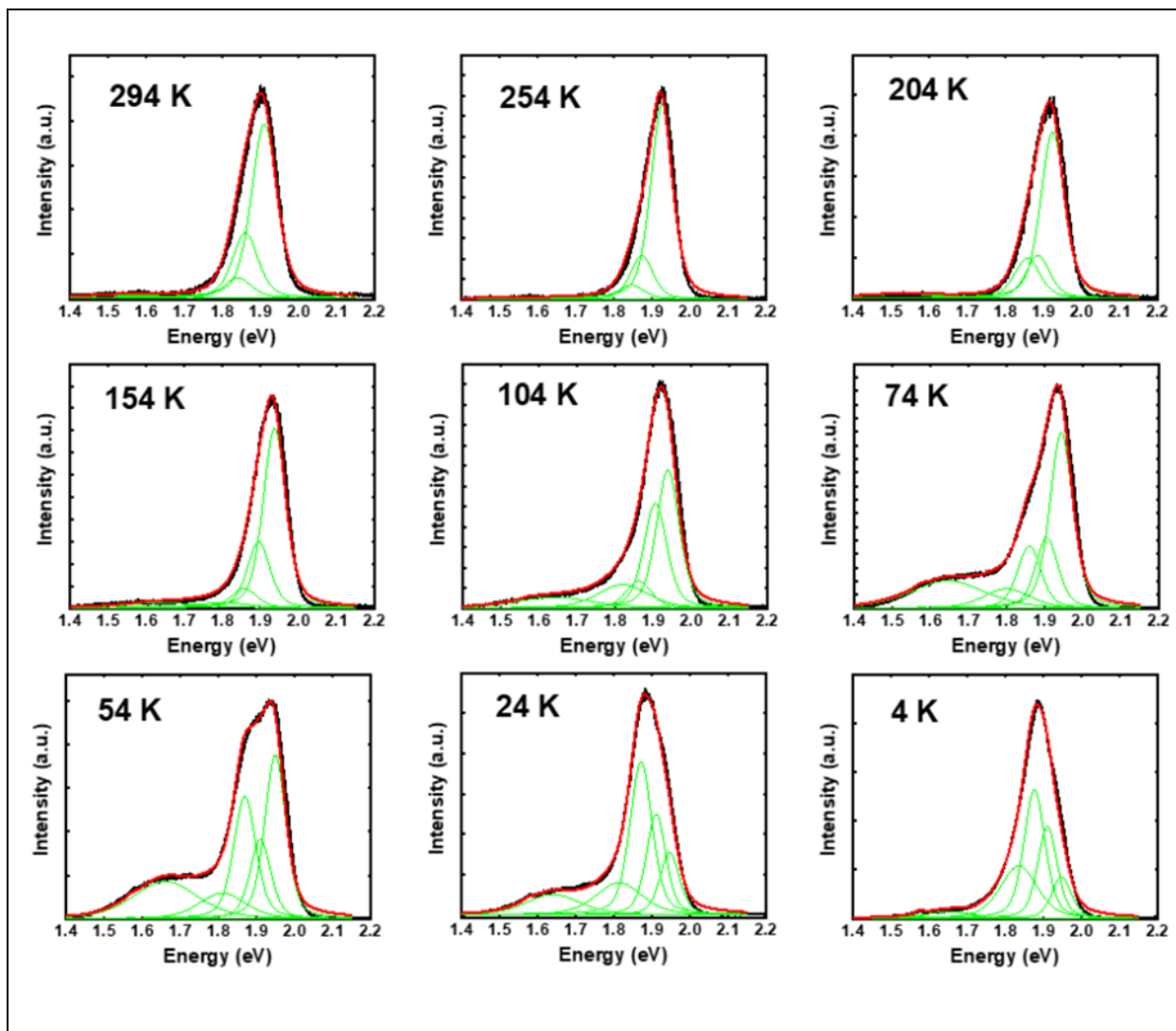


Figure SI 6. PL spectra from intermediate region (MoW-side) of alloyed $\text{Mo}_x\text{W}_{1-x}\text{S}_2$ at different temperatures ranging from 4 K to 300 K. The spectra are deconvoluted with six pseudo-Voigt peaks below 104 K and four peaks above 104 K.

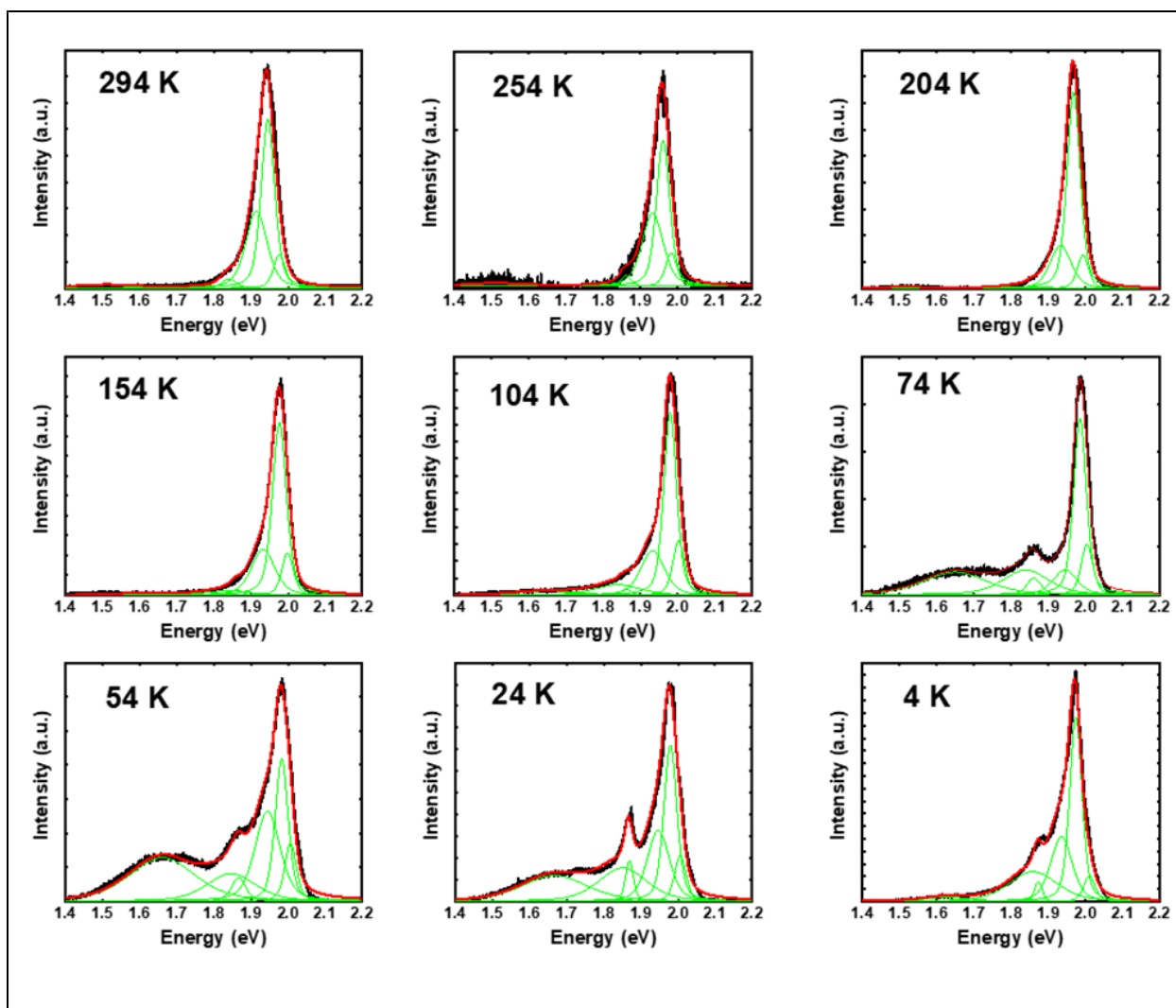


Figure SI 7. PL spectra from W-rich side of alloyed $\text{Mo}_x\text{W}_{1-x}\text{S}_2$ at different temperatures ranging from 4 K to 300 K. The spectra are deconvoluted with six pseudo-Voigt peaks below 104 K and five peaks above 104 K.

Comparison of PL spectra at low T and room T of different regions of alloyed monolayer

$\text{Mo}_x\text{W}_{1-x}\text{S}_2$

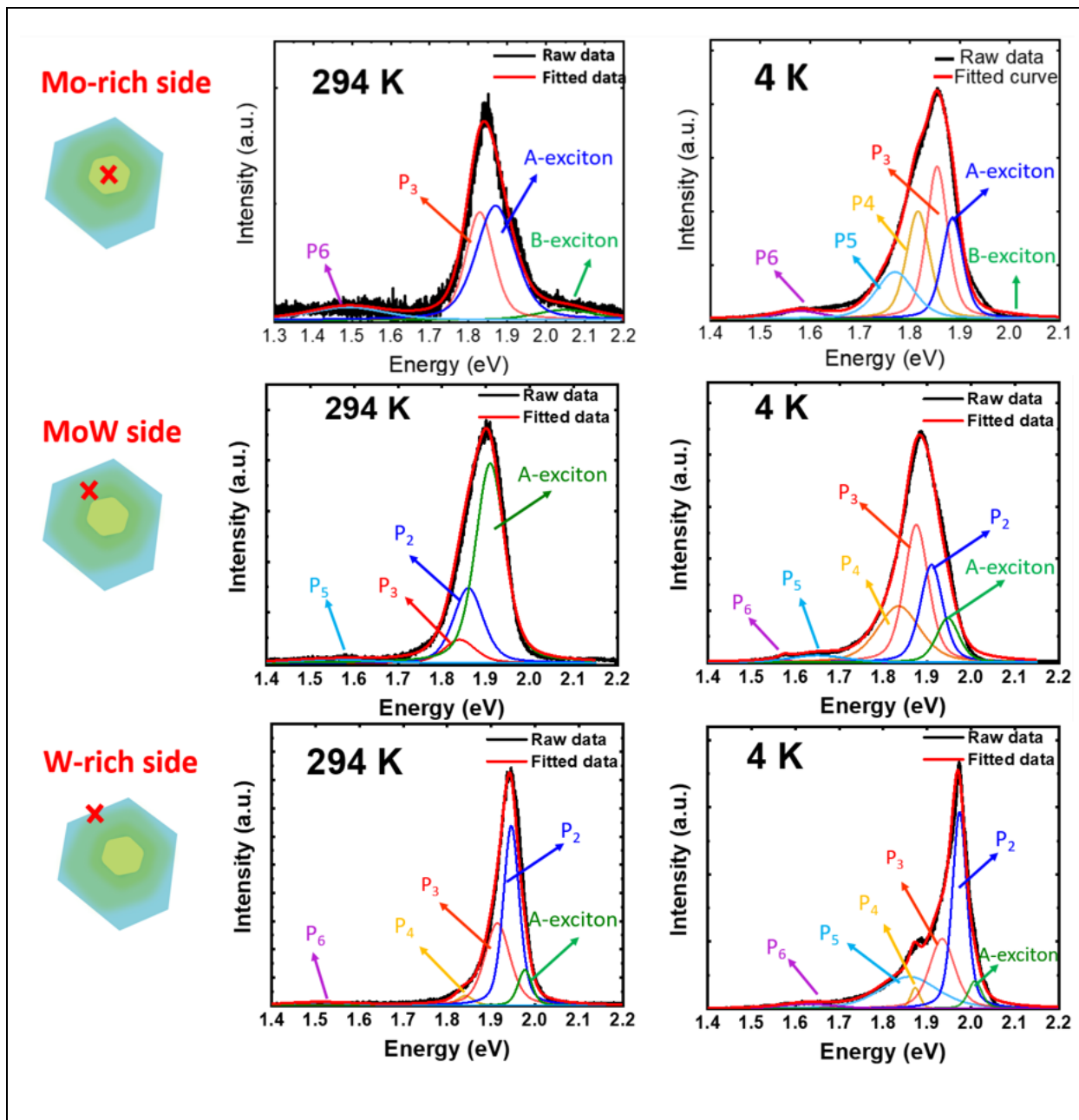


Figure SI 8. Comparison of PL spectra at low T and room T of three different regions of alloyed $\text{Mo}_x\text{W}_{1-x}\text{S}_2$.

Power dependence for Pristine MoS₂ and pristine WS₂ at low T

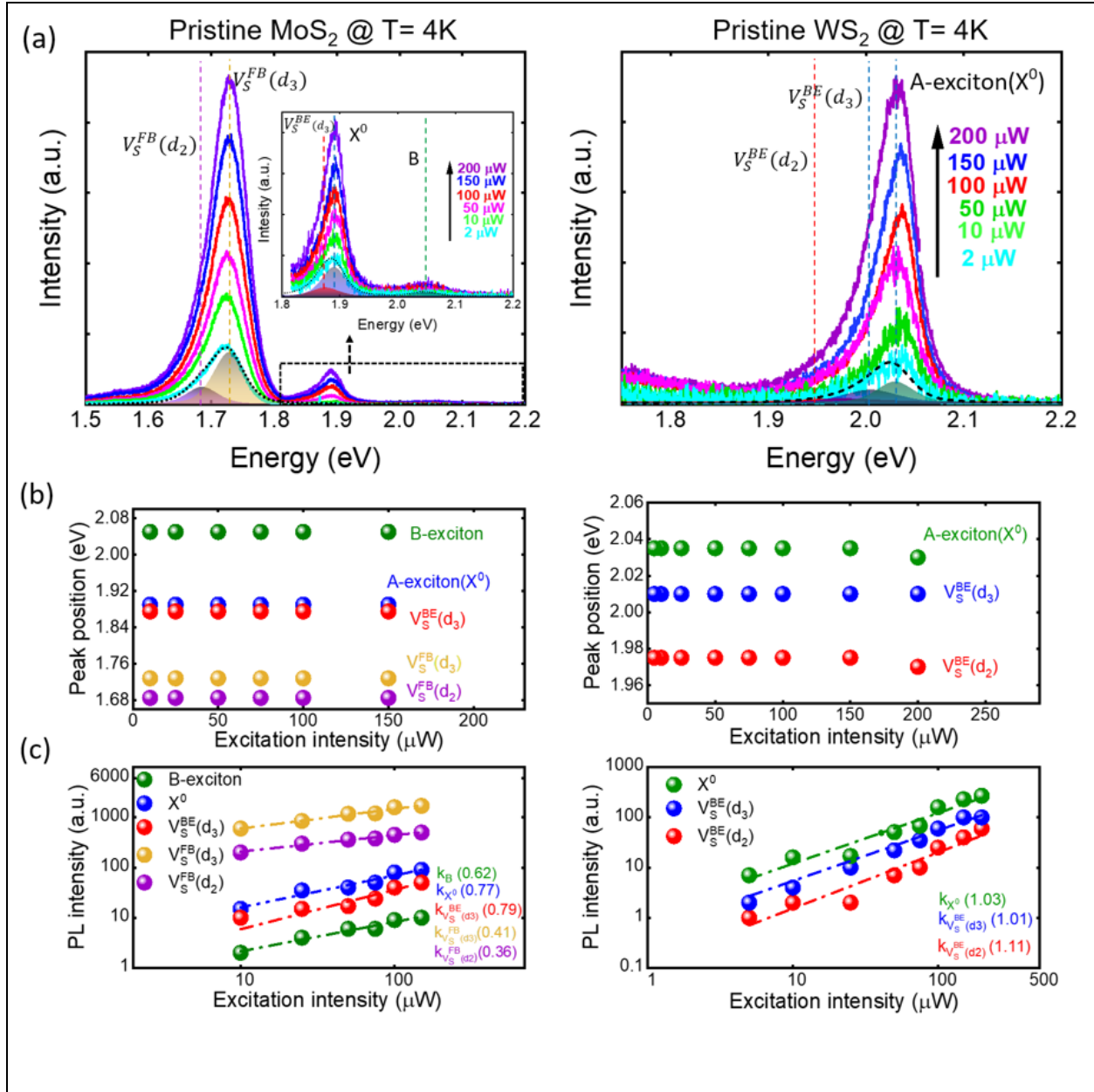


Figure SI 9. Power dependence for pristine MoS₂ and pristine WS₂ monolayers at T = 4 K. (a) Shows the dependence spectra at different excitation powers. (b) Power dependence of peak position for fitted data of PL spectra. (c) Intensity of emission peaks at different excitation powers for fitted data of PL spectra.

To understand the effect of the alloy on exciton emission and benchmark the alloy spectra, we performed power-dependent PL spectroscopy on pristine MoS₂ and WS₂ that were grown using identical CVD approach to that of the alloyed ones used above. The experiments were performed at low temperature (T = 4 K) and similar laser excitation parameters (wavelength and power) as in the case of for Mo_xW_{1-x}S₂ were used. Figure SI 9 shows the PL spectra and analysis for both pristine WS₂ and MoS₂ acquired using excitation laser power from 2 μW to 200 μW. For pristine WS₂, the PL spectra were deconvoluted using three pseudo-Voigt spectral shapes. We identify the three peaks with neutral A-exciton (2.04 eV), $V_S^{BE}(d_3)$ at 2.01 eV, and $V_S^{BE}(d_2)$ at 1.95 eV as summarized in Table 1 in the main article. A similar analysis using five pseudo-Voigt spectral shapes for MoS₂ identifies the intrinsic excitonic peaks, B exciton (2.05 eV), and A exciton (1.895 eV), and a bound exciton associated with V_S level d₃, $V_S^{BE}(d_3)$ (1.875 eV) (Table 1 of the main article). It is interesting to note that the free-to-bound transitions associated with V_S ($V_S^{FB}(d_3)$ and $V_S^{FB}(d_2)$) dominate the radiative process relative to the intrinsic excitons at low temperature. Similar dominant low energy transitions that have been observed previously were attributed to excitons bound to defects or impurities.^{4,5} However, in this study, based on the observed sublinear excitation dependence of the peaks, they are assigned to free-to-bound transitions from the doublet V_S states.

Power dependence of FWHM for pristine MoS₂ and pristine WS₂ at T = 4 K

We have plotted the FWHM of different fitted data for both pristine MoS₂ and WS₂ (Fig. SI 10). in MoS₂. The FWHM of A-exciton is considerably broader than what is reported for exfoliated ML MoS₂⁶. The FWHM of A-exciton (~40 meV) for pristine WS₂ at low temperature is considerably broader than what has been reported for exfoliated ML WS₂ (@ 7K, 18 meV)⁶ and

also broader than CVD grown WS₂ previously reported value of 23 meV at 77K⁷. In both MoS₂ and WS₂ the broadening can be attributed to inhomogeneous broadening caused perhaps by various factors such as doping, defects, strain, substrate effects.

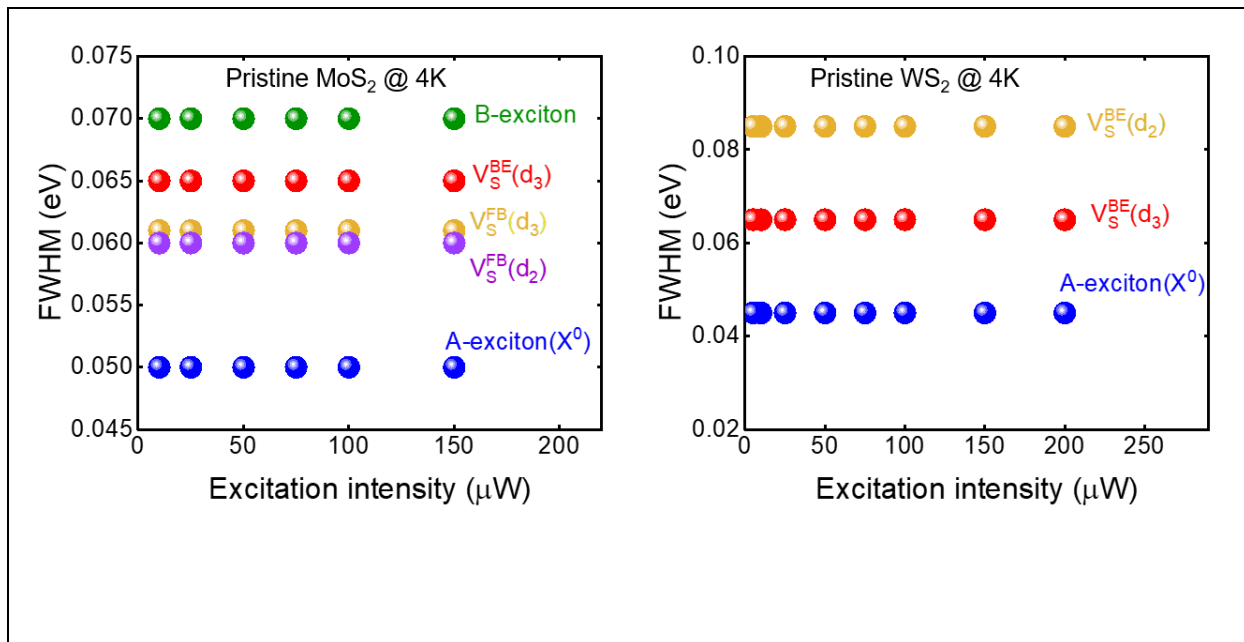


Figure SI 10. Power dependence of FWHM for different peaks of pristine MoS₂ and WS₂ showing negligible effect.

Power dependence for Pristine MoS₂ and pristine WS₂ at room T

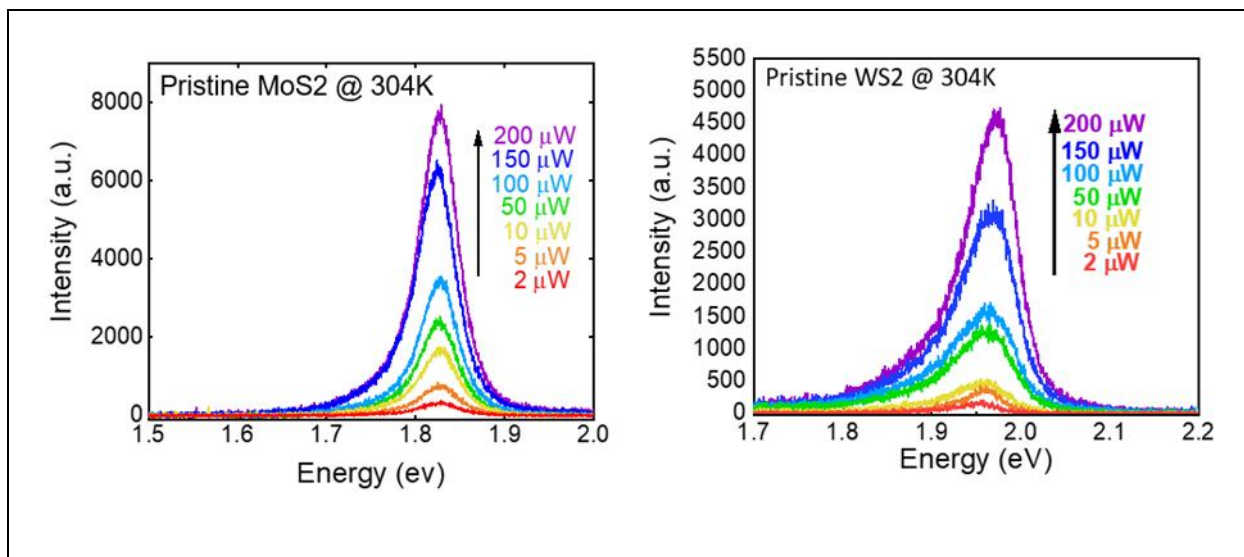


Figure SI 11. Power dependence of pristine WS₂ and MoS₂ at T = 304 K.

Temperature dependence of PL for pristine MoS₂ and WS₂

We also performed temperature-dependent PL spectroscopy of the pristine MoS₂ and WS₂ samples. The experiments were performed in the temperature range of 4 K to 304 K. Figures SI 12 and SI 13 show the PL spectra and analysis of temperature dependence for pristine MoS₂ and WS₂, respectively. At room temperature (T = 304 K), fitting the spectral shape to pseudo-Voigt function yields the peak positions of the B-exciton at 2.01 eV and A-exciton (X⁰) at 1.83 eV. Two other peaks at 1.79 eV and 1.71 eV are attributed to bound excitons associated with the doublet state of V_S (see DFT calculations)⁸. As the temperature is decreased, at 104K there is the evolution of a broad band at 1.7 eV which decomposes to two peaks at 4K which are attributed to free-to-bound transitions from the same doublet state of V_S wherein a photoexcited electron is captured at the defect level and recombines radiatively with a hole in the valence band. Due to the reduced thermal ionization of the captured electron at low temperatures, the free-to-bound

transitions, labelled as $V_S^{FB}(d_3)$ and $V_S^{FB}(d_2)$, are prominent at 4K. In fact, they are the dominant transitions at 4K relative to the excitonic transitions. The intensity of the A-exciton remains almost constant as a function of temperature as shown in Fig. SI 15. For pristine WS₂, at room temperatures, the PL spectra can be fitted using three peaks at 1.963 eV (A-exciton), and two bound exciton transitions peaks $V_S^{BE}(d_3)$ and $V_S^{BE}(d_2)$ with energy levels at 1.897 eV, and 1.85 eV (Fig. SI 13) which are in a good agreement with reported values⁹⁻¹¹.

As temperature decreases, the PL peaks show a blueshift. Figure SI 14 (b) shows the PL peak positions at different temperatures for both pristine MoS₂ and WS₂. The temperature dependence of the PL peaks can be fitted in accordance with Eq. (2) shown in the main article. In Table SI 3 are shown the fitting parameters for the A-exciton, $V_S^{BE}(d_3)$ and $V_S^{BE}(d_2)$ bound excitons for pristine MoS₂ and WS₂, and the values of the average phonon energies are comparable with that of alloy Mo_xW_{1-x}S₂.

Temperature dependence of PL for pristine MoS₂

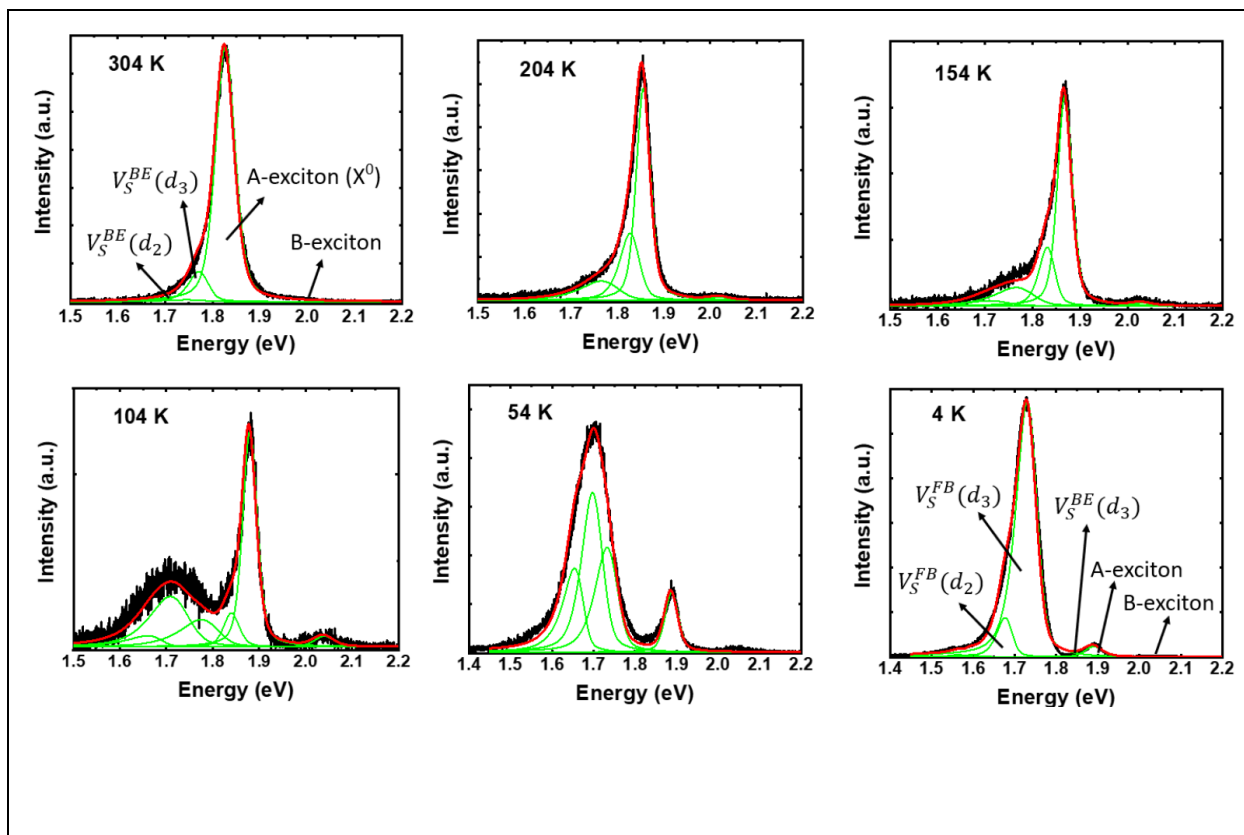
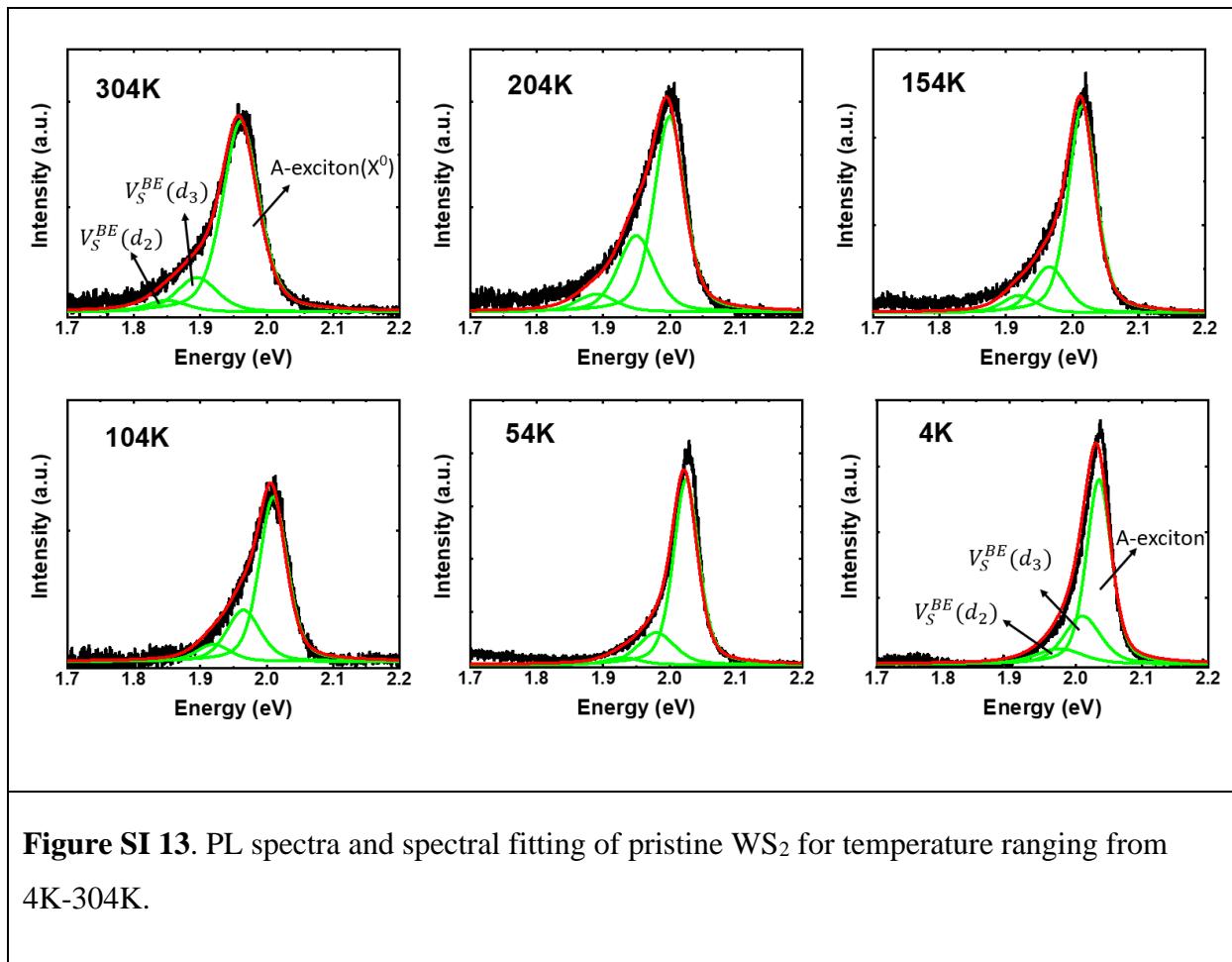


Figure SI 12. PL spectra and spectral fitting of pristine MoS₂ for temperature ranging from 4K-304K.

Temperature dependence of PL for pristine WS₂



Comparison of temperature dependence of PL spectra for pristine MoS₂ and pristine WS₂

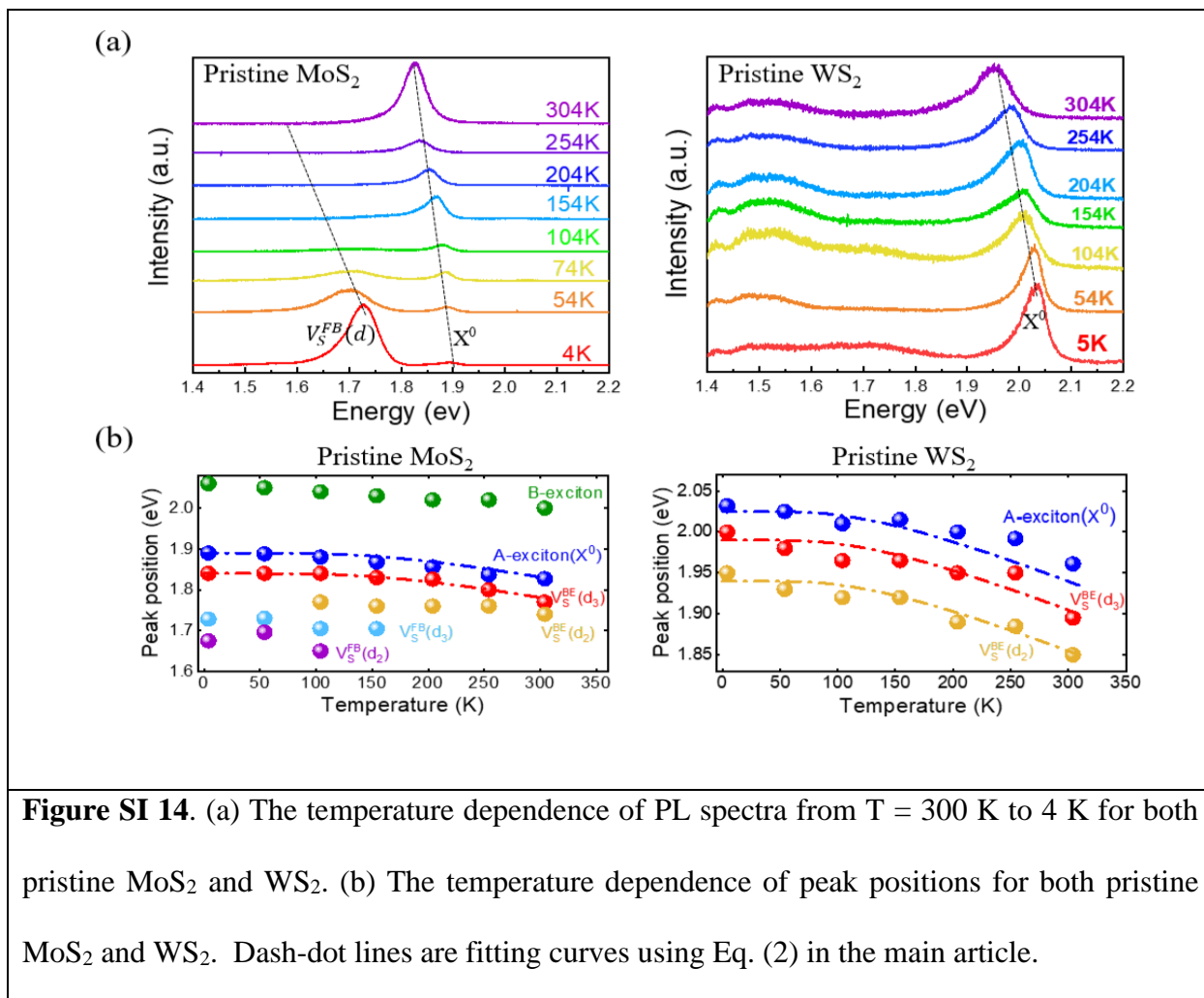


Figure SI 14. (a) The temperature dependence of PL spectra from $T = 300$ K to 4 K for both pristine MoS₂ and WS₂. (b) The temperature dependence of peak positions for both pristine MoS₂ and WS₂. Dash-dot lines are fitting curves using Eq. (2) in the main article.

Temperature dependence of FWHM for pristine MoS₂, WS₂

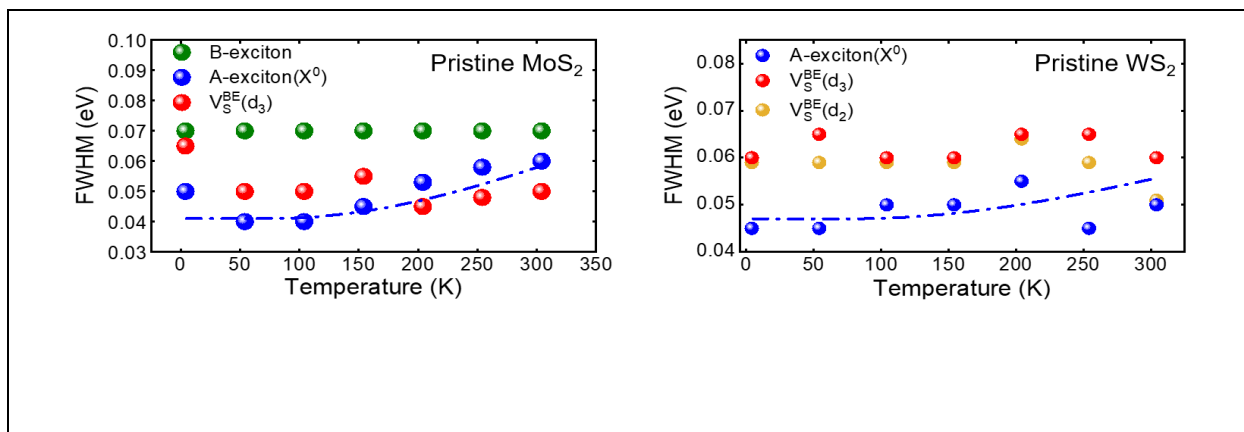


Figure SI 15. Temperature dependence of FWHM for different peaks of pristine MoS₂ and WS₂ with dash-dot curved lines are fitted data using Eq. (1).

Temperature dependence of intensity for pristine MoS₂, WS₂

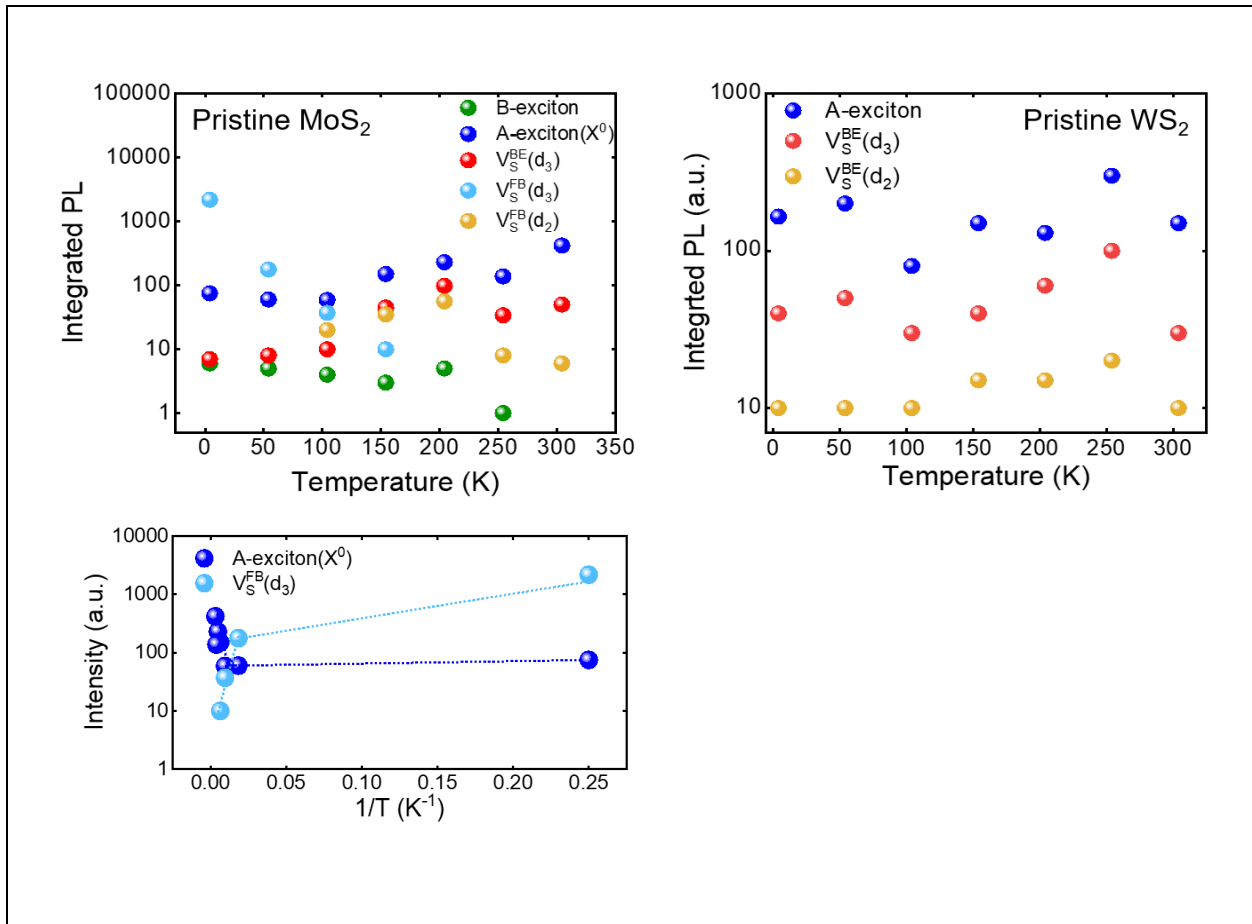


Figure SI 16. Temperature dependence of Intensity for different peaks of pristine MoS₂ and WS₂.

Compilation of peak energies of A-exciton and B-exciton of monolayer WS₂ and MoS₂.

Optical transitions from monolayer WS₂ and MoS₂ have been rigorously studied by several groups at low temperature as well as room temperature. The observed peak position of A-exciton varies over a wide range from ~ 1.90 eV to 1.96 eV in MoS₂ (Tables SI 2) and from ~ 2.01 eV to 2.10 eV in WS₂ (Table SI 1). On the low energy side of the A-exciton an optical transition in the range 1.88 eV to 1.92 eV in MoS₂ and 1.96 eV to 2.05 eV in WS₂ is typically attributed to A⁻ trion. Since the intensity of the optical transition in these above energy ranges show linear dependence on excitation intensity as opposed to a $3/2$ dependence expected for a three particle trion transition, the involvement of a trion in the radiative process is not unambiguous. It is to be noted that optical transitions on the low energy side of the A-exciton have also been assigned to defect/impurity related bound excitons (See Tables SI 1 and SI 2). In this work we have attributed the low energy transitions to V_S defects.

Table SI 1. The summary of PL transition energies associated with A⁻ trion, A-exciton, and defects in monolayer WS₂.

Article	A ⁻ trion (eV)	A-exciton (eV)	B-exciton (eV)	Defect (eV)
Krustok et.al ¹⁵ @ 10K_CVD	1.97	2.02	-	1.94
Wan et. al ¹⁶ @ 4K_CVD	2.02	2.08	-	1.98
Kaupmees ¹⁷ et. al @15K_CVD	1.96	2.01	-	-
Plechinger et.al ¹¹ @ 4K_exfoliated	2.04	2.09	-	-
Jadczak et.al ⁶ @ 7K_exfoliated	2.05	2.10	-	-
This work @ 4K (pristine WS ₂)	-	2.04	-	-
This work @ 4K (alloyed monolayer Mo _x W _{1-x} S ₂ , W-rich side)	-	2.01	-	1.94-1.871.86-1.63

Table SI 2. The summary of PL transition energies associated with A⁻ trion, A-exciton, B-exciton and defects in monolayer MoS₂.

Article	A ⁻ trion (eV)	A-exciton (eV)	B-exciton (eV)	Defect (eV)
Mak et.al ¹² @ 10K	1.90	1.92	-	-
Jadczak et.al ⁶ @ 7K_exfoliated	1.92	1.96	-	-
Cadiz et.al ¹⁸ @ 10K	1.92	1.96	-	-
Pei et.al ¹⁹ @ 10K	1.88	1.92	-	-
Sharma et.al ¹³ @ 4K_CVD	1.88	1.92	2.08	1.80-1.87
Verhagen et.al ⁴ @ 10K_CVD	1.87	1.89	1.96	1.73-1.78
Panday et.al ¹⁴ @ 4K_exfoliated	1.92	1.96	2.08	1.82
Christopher et.al ²⁰ @ 83K	1.92	1.95	2.09	--
This work @ 4K (pristine MoS ₂)	-	1.895	2.05	1.73-1.68
This work @ 4K (alloyed monolayer Mo _x W _{1-x} S ₂ , Mo-rich side)	-	1.89	2.01	1.82-1.77-1.58

Table SI 3. Fitted Values of the Exciton–Phonon Coupling Strength, S, the Average Phonon Energy, $\langle \hbar\omega \rangle$, and $E_{g(0)}$ of neutral A exciton, $V_S^{BE}(d_3)$ and $V_S^{BE}(d_2)$ for different regions of alloyed monolayer Mo_xW_{1-x}S₂ compared to pristine MoS₂ and WS₂.

	Pristine MoS ₂	Pristine WS ₂	Mo-rich side of alloyed Mo _x W _{1-x} S ₂	MoW side of alloyed Mo _x W _{1-x} S ₂	W-rich side of alloyed Mo _x W _{1-x} S ₂
E_{0A} (eV)	1.89	2.04	1.90	1.96	2.01
$V_S^{BE}(d_3)$ (eV)	1.84	1.99		1.91	1.98
$V_S^{BE}(d_2)$ (eV)		1.94	1.862	1.875	1.95
$\langle \hbar\omega \rangle$ (meV)	50	35	50	35	44
S	3.5	3.5	1.91	2.2	2.2

Raman and PL Spectra at room temperature of alloyed Mo_xW_{1-x}S₂ monolayer

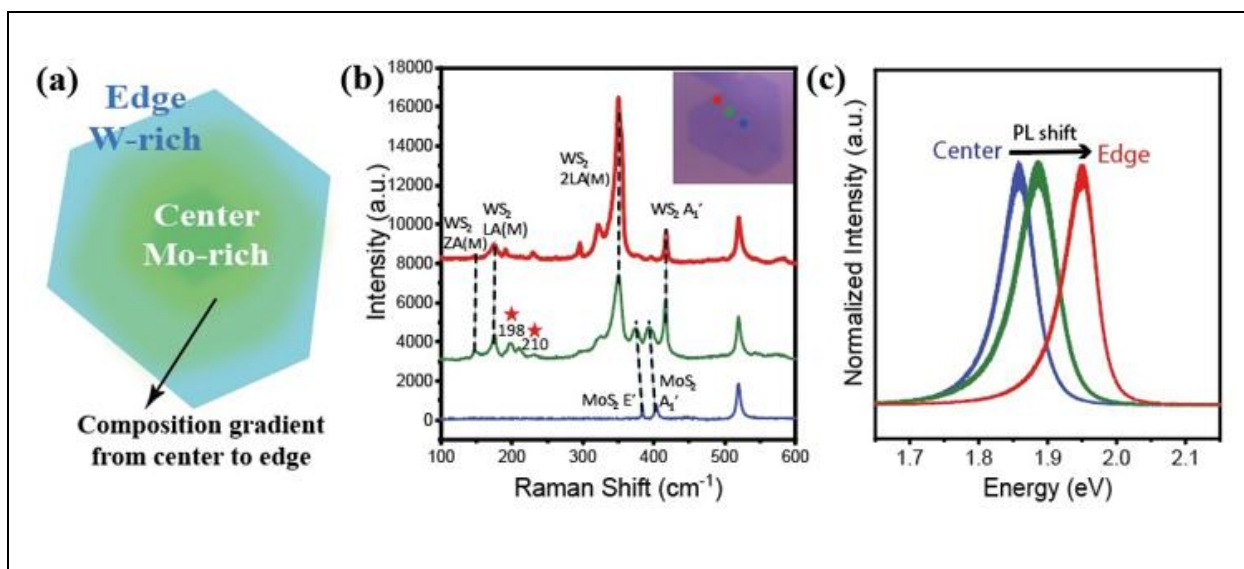


Figure SI 17. Far-Field Optical Characterization of alloyed monolayer $\text{Mo}_x\text{W}_{1-x}\text{S}_2$. (a) Schematic of the structure of alloyed monolayer $\text{Mo}_x\text{W}_{1-x}\text{S}_2$. (b) Raman and (c) PL spectra of various regions in alloyed monolayer $\text{Mo}_x\text{W}_{1-x}\text{S}_2$. The excitation laser is at 532 nm.

DFT calculations

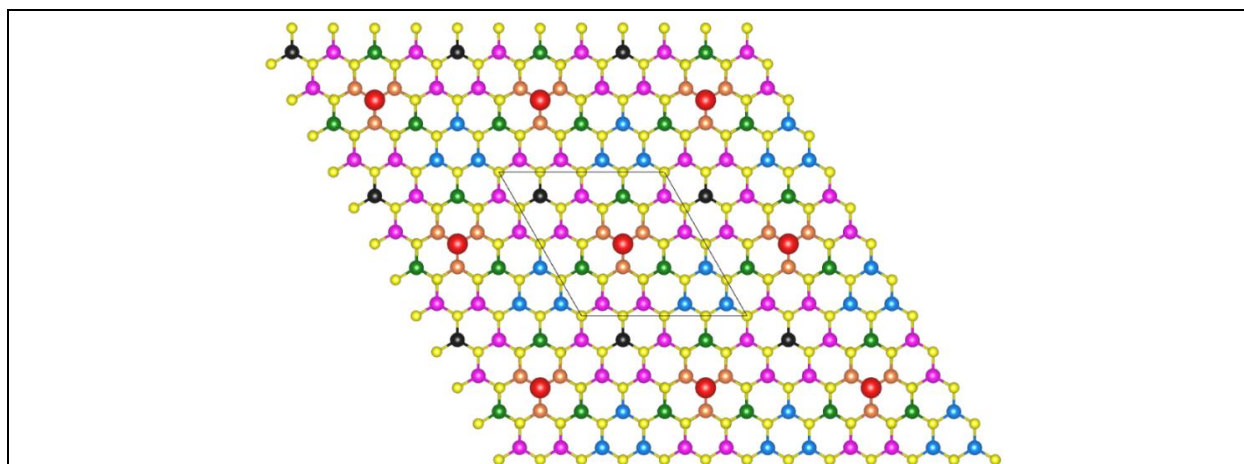


Figure SI 18. The $4 \times 4 \times 1 \text{ Mo}_{16}\text{W}_{16(1-x)}\text{S}_{31}$ supercell (bounded by black lines) illustrating all possible C_{3v} symmetric structures. The large red atoms are situated at the position of the S vacancies to emphasize their placement and the other colors (orange, green, pink, teal, and black) represent the position that a transition metal (Mo or W) can be situated to generate the 32 possible structures ($5 \text{ distinct colors with } 2 \text{ possible atoms each yields } 2^5 = 32 \text{ structures}$).

For all transitions, the corrected energy ($E_{g(A,B)}^{corr}$) for the alloys is determined from the equation:

$$E_{g(A,B)}^{corr} = E_g \left[\frac{E_{EXP(A,B)}^{MoS_2}}{E_{PBE(A,B)}^{MoS_2}} x + \frac{E_{EXP(A,B)}^{WS_2}}{E_{PBE(A,B)}^{WS_2}} (1 - x) \right] \quad (2)$$

where x is the Mo concentration and E_g is the PBE calculated A (B) exciton transition energy, $E_{PBE(A,B)}^{MoS_2} = 1.615$ eV (1.759 eV) and $E_{PBE(A,B)}^{WS_2} = 1.607$ eV (2.001 eV) are the PBE calculated transition energies for $Mo_{16}S_{32}$ and $W_{16}S_{32}$, respectively, for the A (B) exciton energies. Similarly, $E_{EXP(A,B)}^{MoS_2} = 1.88$ eV (2.02 eV) and $E_{EXP(A,B)}^{WS_2} = 2.02$ eV (2.40 eV) are the experimental A (B) exciton energies for pristine $Mo_{16}S_{32}$ and $W_{16}S_{32}$, respectively^{21,22}. For defect-related transitions, the same correction applied to the A [B] exciton transitions, is applied to the spin-down (red-red, $v-d_2$, $v-d_3$) [spin-up, (blue-blue, v_i-d_1 , v_i-d_4)] transitions. The valence band splitting can be represented by the linear relationship described by Vegard's law²³ which is expressed in terms of the Mo concentration (x) as

$$E_v(x) = xE_{v,Mo_{16}S_{31,32}} + (1 - x)E_{v,W_{16}S_{31,32}} \quad (3)$$

where $E_{v,Mo_{16}S_{31,32}}$ and $E_{v,W_{16}S_{31,32}}$ represent the valence (v) band splitting for non-defective ($Mo_{16}S_{32}$ and $W_{16}S_{32}$) and V_S defective ($Mo_{16}S_{31}$ and $W_{16}S_{31}$) transition metal dichalcogenides. In the cases of the A and B exciton transition energies and conduction band splitting, the relationship becomes quadratic due to the introduction of a bowing parameter (b), which is described by the relationship:

$$E_{g,c}(x) = xE_{g,c,Mo_{16}S_{31}} + (1-x)E_{g,c,W_{16}S_{31}} - bx(1-x) \quad (4)$$

where $E_{g,Mo_{16}S_{31,32}}$ and $E_{g,W_{16}S_{31,32}}$ are the transition energies for $Mo_{16}S_{31,32}$ and $W_{16}S_{31,32}$, respectively, and similarly $E_{c,Mo_{16}S_{31,32}}$ and $E_{c,W_{16}S_{31,32}}$ are the conduction band splitting for $Mo_{16}S_{31,32}$ and $W_{16}S_{31,32}$, respectively. This analysis reveals a strong linear correlation for the valence band splitting as a function of the Mo concentration, but there is bowing observed for the A and B excitons and the conduction band splitting (Fig. 5 and Fig. SI 20). As the Mo concentration increases in the pristine $[Mo_{16x}W_{16(1-x)}S_{32}]$ alloys, the A and B exciton decreases quadratically (see Fig. 5). The defect-mediated transitions are shown in an example with the band structure of an $Mo_7W_9S_{31}$ with the $v-d_2$, $v-d_3$, v_i-d_1 , and v_i-d_4 transitions which are referred to as R_1 , R_2 , B_1 , and B_2 , respectively (Fig. SI 19).

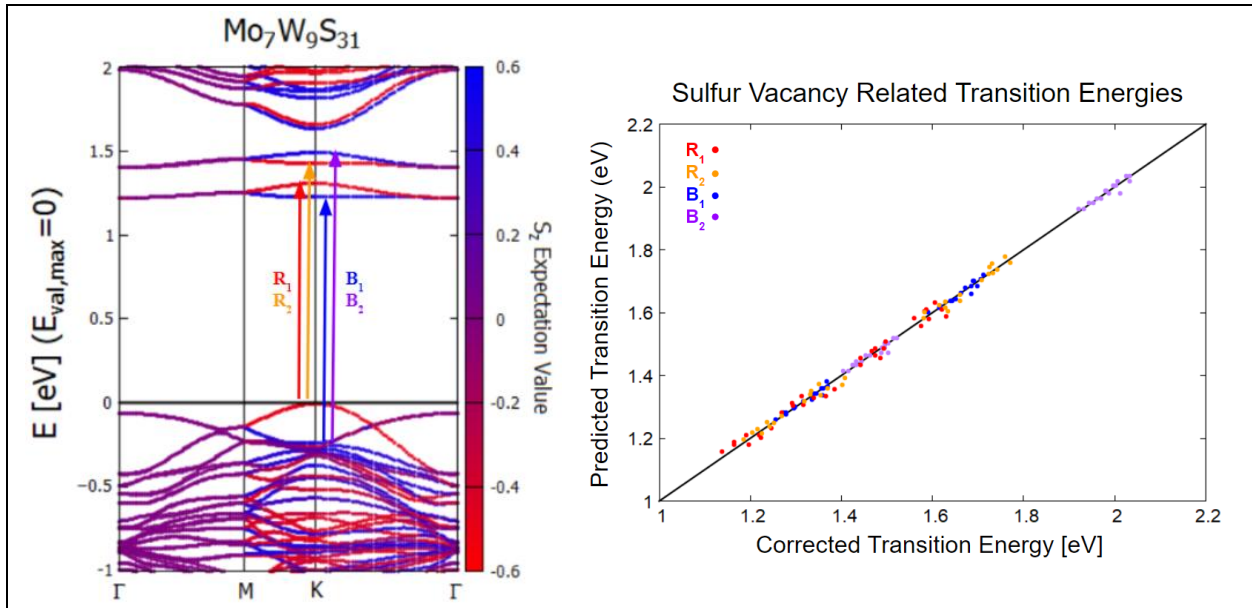


Figure SI 19. The $Mo_7W_9S_{31}$ band structure calculated using the PBE functional is used as an example to illustrate the position of the defect-mediated energy levels in the alloy [left]. In this case, only the R_1 and R_2 and B_1 and B_2 defect-mediated transitions are shown. [right] The predicted defect-related transition energies are plotted against the shifted energy from the

energies calculated using the PBE functional with the identity line (essentially $f(x) = x$) shown as a black line.

In order to create a model to predict the defect-mediated transition energies, a parameter (t_i) is introduced where $t_i = -1$ or 1 based on which atom (Mo or W) occupies the corresponding-colored position (from Fig. SI 18) where $t_i = -1$ for Mo atoms and $t_i = 1$ for W atoms. The best fit equation for this model is applied to the five sets of colored atoms [black (B), pink (P), teal (T), green (G), and orange (O)] to create a linear combination, which is represented by

$$E_{trans} = b + a_B t_B + a_P t_P + a_T t_T + a_G t_G + a_O t_O \quad (5)$$

where b , E_{trans} , and a_i represent a constant, particular transition (B_1 , R_1 , R_2 , and B_2), and weighting coefficient corresponding to a specific color (i) from Fig. SI 19, respectively. Based on the 32 possible structures investigated, the best-fitting linear combinations generated for the B_1 , R_1 , R_2 , and B_2 transitions are

$$E_{B1} = 1.491 - 0.008t_B - 0.031t_P + 0.011t_T + 0.010t_G + 0.171t_O \quad (6)$$

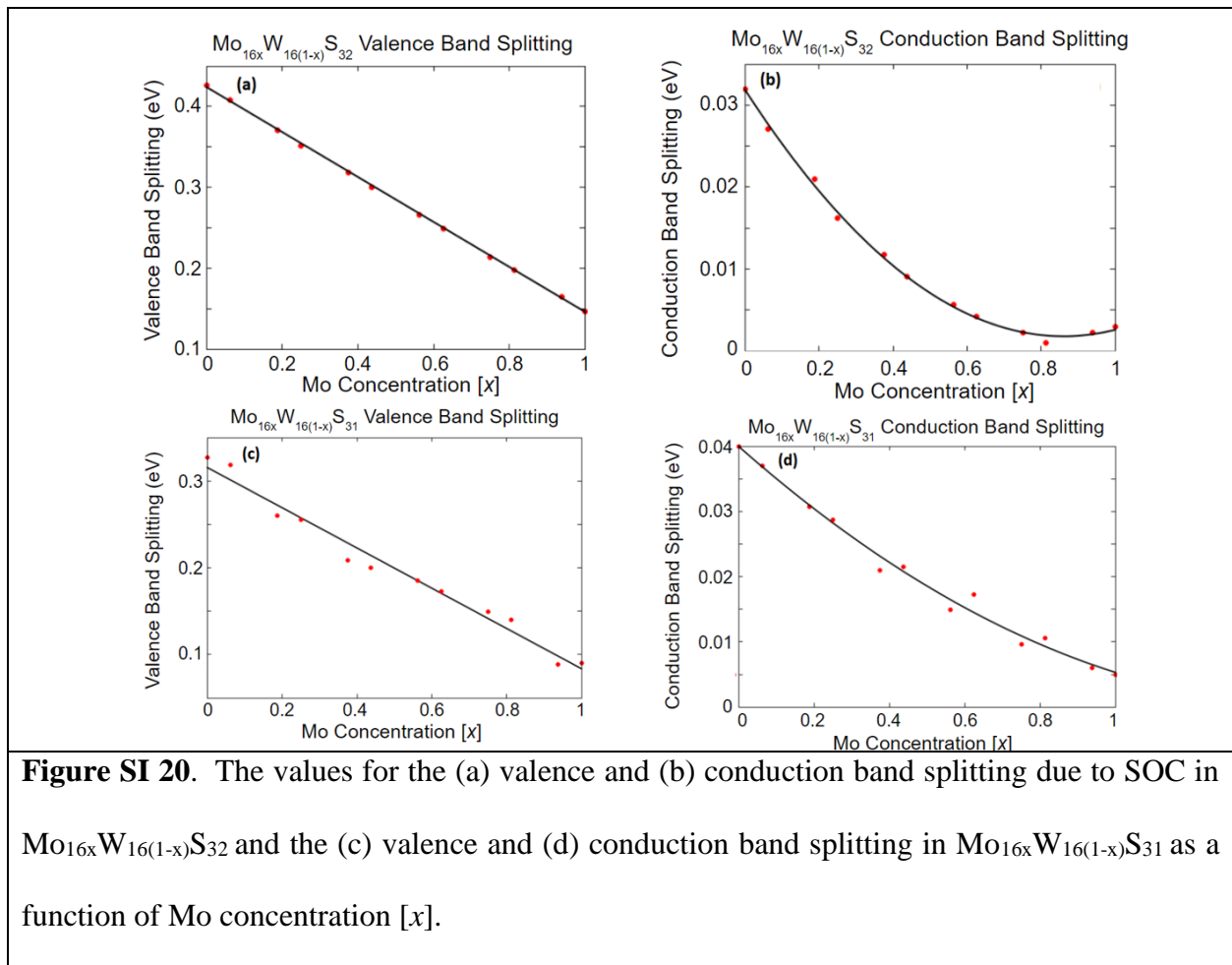
$$E_{R1} = 1.395 - 0.011t_B - 0.063t_P - 0.015t_T - 0.011t_G + 0.138t_O \quad (7)$$

$$E_{R2} = 1.487 - 0.011t_B - 0.061t_P - 0.010t_T - 0.016t_G + 0.193t_O \quad (8)$$

$$E_{B2} = 1.725 - 0.029t_P + 0.009t_T + 0.015t_G + 0.258t_O \quad (9)$$

In general, the placement of atoms near V_S (or orange position) has the strongest effect with the placement of W atoms tending to increase the defect-mediated transition energies. For all cases regarding the defect-mediated transitions, the presence of W atoms at the pink and black positions tends to decrease the transition energy. For the spin-down (red) transitions, the presence of W

atoms at the green and teal positions tends to decrease the transition energies, while for the spin-up (blue) transitions, the presence of W atoms at the green and teal positions tends to increase the transition energies. Additionally, the difference between the d_2 and d_3 energy levels becomes significantly larger when V_S is adjacent to W atoms, but when the vacancy is adjacent to Mo atoms, then the difference becomes significantly smaller (Fig. SI 21). Overall, this model predicts the defect-mediated transition energies very well with strong correlation ($R^2 = 0.996$) with predictions residing very close to the identity line.



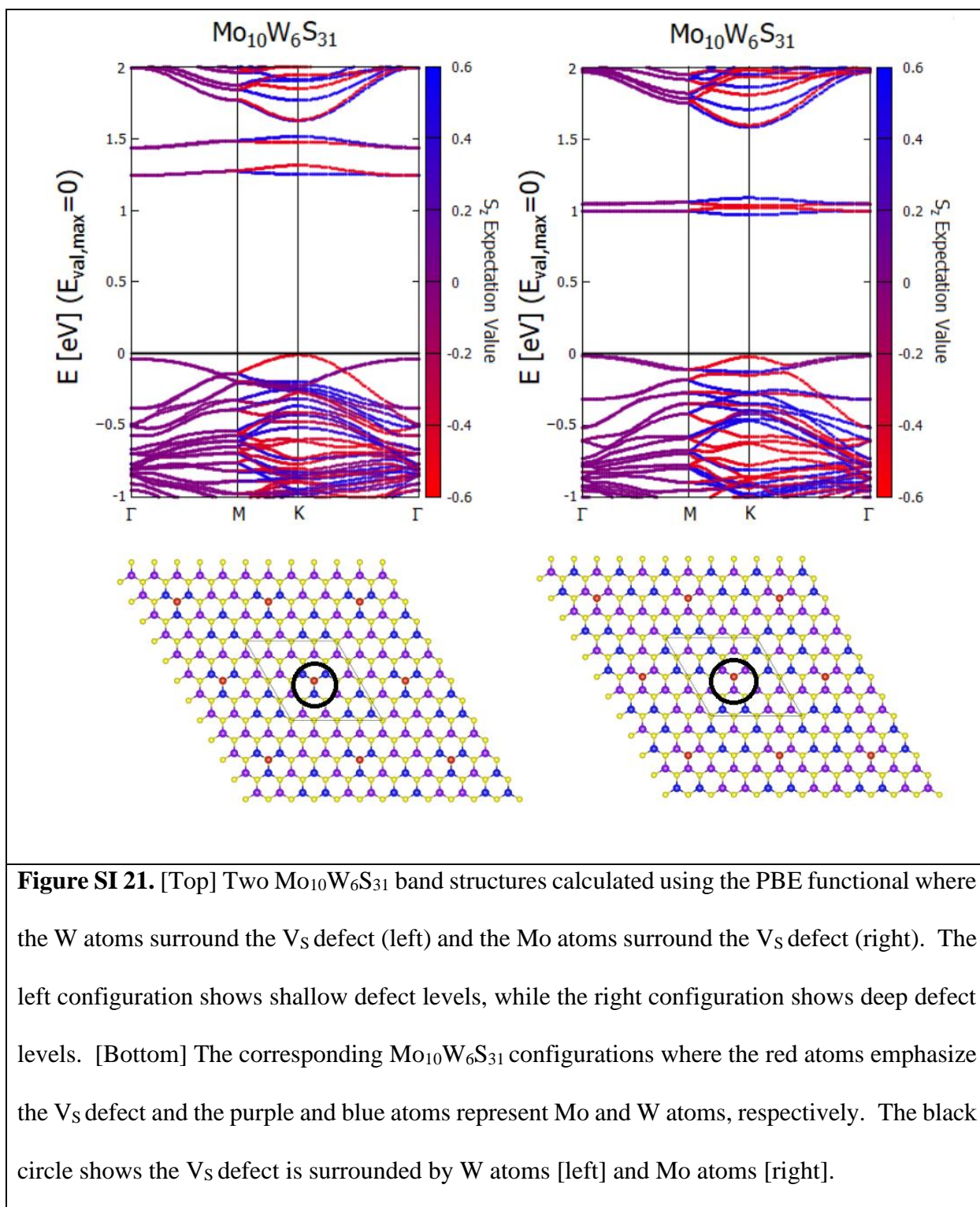


Table SI 4. The averages for the corrected transition energies [R_1 , R_2 , B_1 , and B_2] for both when the V_S defect is surrounded by W atoms (W) and by Mo atoms (Mo) for each the W-rich ($x \leq 0.25$), MoW (intermediate, $0.25 < x < 0.75$), and Mo-rich ($x \geq 0.75$) regions. The experimentally observed peaks far from the band edge (P5, P6) that best match the transitions R_1 and R_2 are shown, respectively, as $R_1(\text{exp})$ and $R_2(\text{exp})$. Since the transitions involving the spin-orbit split valance band such as the B-excitons are generally weaker than the A-excitons (as in MoS_2) or not even observed (as in WS_2), no assignment is made to the transitions B_1 and B_2 involving the spin-orbit split valance band (see Fig. SI 20).

Region	R_1	R_2	B_1	B_2	$R_1(\text{exp})$	$R_2(\text{exp})$
W-rich (W)	1.44-1.49	1.58-1.66	1.62-1.69	1.94-2.01	-	P6
MoW (W)	1.48-1.63	1.63-1.77	1.59-1.71	1.92-2.03	P6	P5
Mo-rich (W)	1.59-1.61	1.73-1.76	1.66-1.67	1.98	P6	P5
W-rich (Mo)	1.14-1.16	1.19-1.20	1.30-1.32	1.45-1.46	-	-
MoW (Mo)	1.17-1.29	1.22-1.33	1.25-1.37	1.40-1.52	-	-
Mo-rich (Mo)	1.29-1.39	1.33-1.41	1.33-1.36	1.49-1.50	-	-

Supplementary References

- 1 Dey, P. *et al.* Optical Coherence in Atomic-Monolayer Transition-Metal Dichalcogenides Limited by Electron-Phonon Interactions. *Phys Rev Lett* **116**, 127402 (2016). <https://doi.org/10.1103/PhysRevLett.116.127402>
- 2 Stevens, C. *et al.* in *Journal of Physics: Conference Series*. 012035 (IOP Publishing).

- 3 Rudin, S., Reinecke, T. L. & Segall, B. Temperature-dependent exciton linewidths in semiconductors. *Phys Rev B Condens Matter* **42**, 11218-11231 (1990). <https://doi.org/10.1103/physrevb.42.11218>
- 4 Verhagen, T., Guerra, V. L. P., Haider, G., Kalbac, M. & Vejpravova, J. Towards the evaluation of defects in MoS₂ using cryogenic photoluminescence spectroscopy. *Nanoscale* **12**, 3019-3028 (2020). <https://doi.org/10.1039/c9nr07246b>
- 5 Akmaev, M. *et al.* Spatiotemporal dynamics of free and bound excitons in CVD-grown MoS₂ monolayer. *Applied Physics Letters* **119**, 113102 (2021).
- 6 Jadcak, J. *et al.* Probing of free and localized excitons and trions in atomically thin WSe₂, WS₂, MoSe₂ and MoS₂ in photoluminescence and reflectivity experiments. *Nanotechnology* **28**, 395702 (2017). <https://doi.org/10.1088/1361-6528/aa87d0>
- 7 Carozo, V. *et al.* Optical identification of sulfur vacancies: Bound excitons at the edges of monolayer tungsten disulfide. *Science advances* **3**, e1602813 (2017).
- 8 Mitterreiter, E. *et al.* The role of chalcogen vacancies for atomic defect emission in MoS₂. *Nat Commun* **12**, 3822 (2021). <https://doi.org/10.1038/s41467-021-24102-y>
- 9 Wei, K., Liu, Y., Yang, H., Cheng, X. & Jiang, T. Large range modification of exciton species in monolayer WS₂. *Appl Opt* **55**, 6251-6255 (2016). <https://doi.org/10.1364/AO.55.006251>
- 10 Xu, X. *et al.* Localized state effect and exciton dynamics for monolayer WS₂. *Opt Express* **29**, 5856-5866 (2021). <https://doi.org/10.1364/OE.415176>
- 11 Plechinger, G. *et al.* Identification of excitons, trions and biexcitons in single-layer WS₂. *physica status solidi (RRL) - Rapid Research Letters* **9**, 457-461 (2015). <https://doi.org/10.1002/pssr.201510224>
- 12 Mak, K. F. *et al.* Tightly bound trions in monolayer MoS₂. *Nature Materials* **12**, 207-211 (2013). <https://doi.org/10.1038/nmat3505>
- 13 Sharma, R. *et al.* Spectroscopic correlation of chalcogen defects in atomically thin MoS₂(1-x)Se_{2x} alloys. *Journal of Physics: Materials* **3** (2020). <https://doi.org/10.1088/2515-7639/abab6a>
- 14 Pandey, J. & Soni, A. Unraveling biexciton and excitonic excited states from defect bound states in monolayer MoS₂. *Applied Surface Science* **463**, 52-57 (2019). <https://doi.org/10.1016/j.apsusc.2018.08.205>
- 15 Krustok, J. *et al.* Local strain-induced band gap fluctuations and exciton localization in aged WS₂ monolayers. *AIP Advances* **7** (2017). <https://doi.org/10.1063/1.4985299>
- 16 Wan, Y. *et al.* Low-defect-density WS₂ by hydroxide vapor phase deposition. *Nat Commun* **13**, 4149 (2022). <https://doi.org/10.1038/s41467-022-31886-0>

- 17 Kaupmees, R. *et al.* Tailoring of Bound Exciton Photoluminescence Emission in WS₂ Monolayers. *physica status solidi (RRL)–Rapid Research Letters* **14**, 1900355 (2020).
- 18 Cadiz, F. *et al.* Excitonic linewidth approaching the homogeneous limit in MoS₂-based van der Waals heterostructures. *Physical Review X* **7**, 021026 (2017).
- 19 Pei, J. *et al.* Exciton and trion dynamics in bilayer MoS₂. *Small* **11**, 6384-6390 (2015).
- 20 Christopher, J. W., Goldberg, B. B. & Swan, A. K. Long tailed trions in monolayer MoS₂: Temperature dependent asymmetry and resulting red-shift of trion photoluminescence spectra. *Sci Rep* **7**, 14062 (2017). <https://doi.org:10.1038/s41598-017-14378-w>
- 21 Li, Z. *et al.* Active light control of the MoS₂ monolayer exciton binding energy. *ACS nano* **9**, 10158-10164 (2015).
- 22 Zhu, B., Chen, X. & Cui, X. Exciton binding energy of monolayer WS₂. *Sci Rep* **5**, 9218 (2015). <https://doi.org:10.1038/srep09218>
- 23 Denton, A. R. & Ashcroft, N. W. Vegard's law. *Physical Review A* **43**, 3161-3164 (1991). <https://doi.org:10.1103/PhysRevA.43.3161>